INTERNATIONAL JOURNAL FOR NUMERICAL METHODS IN FLUIDS
Int. J. Numer. Meth. Fluids 2006; **52**:393–432

A 3D second-order accurate projection-based Finite Volume code on non-staggered, non-uniform structured grids with continuity preserving properties: application to buoyancy-driven flows

F. M. Denaro*,†

Dipartimento di Ingegneria Aerospaziale e Meccanica, Seconda Universita' degli Studi di Napoli, Italy

SUMMARY

It is well known that exact projection methods (EPM) on non-staggered grids suffer for the presence of non-solenoidal spurious modes. Hence, a formulation for simulating time-dependent incompressible flows while allowing the discrete continuity equation to be satisfied up to machine-accuracy, by using a Finite Volume-based second-order accurate projection method on non-staggered and non-uniform 3D grids, is illustrated. The procedure exploits the Helmholtz–Hodge decomposition theorem for deriving an additional velocity field that enforces the discrete continuity without altering the vorticity field. This is accomplished by first solving an elliptic equation on a compact stencil that is by performing a standard approximate projection method (APM). In such a way, three sets of divergence-free normal-to-face velocities can be computed. Then, a second elliptic equation for a scalar field is derived by prescribing that its additional discrete gradient ensures the continuity constraint based on the adopted linear interpolation of the velocity. Characteristics of the double projection method (DPM) are illustrated in details and stability and accuracy of the method are addressed. The resulting numerical scheme is then applied to laminar buoyancy-driven flows and is proved to be stable and efficient. Copyright © 2006 John Wiley & Sons, Ltd.

KEY WORDS: finite volume methods; non-staggered grids; continuity constraint; approximate projection methods; buoyancy-driven incompressible flows

1. INTRODUCTION

The hypothesis of fluid incompressibility is traditionally adopted for solving problems in which acoustic waves propagate at a velocity much greater than that of macroscopic advective

---

*Correspondence to: F. M. Denaro, Dipartimento di Ingegneria Aerospaziale e Meccanica, Real Casa dell'Annunziata, Via Roma 29, 81031 Aversa, (CE), Italy.
†E-mail: denaro@unina.it

Contract/grant sponsor: CINECA consortium

Received 17 July 2005
Revised 14 December 2005
Accepted 26 December 2005

transport of properties, which is the case of low Mach number flows. Such hypothesis remains substantially accepted also for flows governed by weak temperature gradients such as buoyancy-driven flows. Hence, even if the hypothesis of incompressibility leads to simplify the Navier–Stokes (NS) equations, the fact that the mass-conservation law reduces to the constraint $\underline{\nabla} \cdot \mathbf{v} = 0$, everywhere and for all time, produces several problems in solving the continuous (hyperbolic in the continuity, parabolic in the momentum and energy equations) as well as discrete formulation of the governing equations, e.g. see Reference [1]. It is well known that the pressure acts only as a Lagrangian multiplier, thus, preserving the continuity constraint is imperative for a well-suited numerical solution whatever the pointwise or integral formulation of the NS equations is adopted. Owing to the advantage in separating velocity and pressure fields, projection methods are often used for solving the incompressible form of the NS equations.

Finite volume (FV) formulations make use of the discretization of the integral form of conservation laws differentiating in this aspect from finite difference (FD) ones wherein the pointwise form is discretized. Generally, FV-based methods are particularly favoured for their species-conservation properties as well as for their feasibility in being applied on both regular and non-regular grids (progresses in this field are highlighted by the old review [2] and the recent book [3]). Besides, staggered (i.e. variables shifted each other in their nodal position) or non-staggered (i.e. variables positioned in the same nodes) grid collocations are possible with both FV and FD formulations. However, since from the appearance of the historical Marker-and-Cell (MAC) FD-based method [4], which ensures discrete mass conservation, staggered grids were prevalently used.

Nevertheless, owing to a greater simplicity of its implementation, the use of non-staggered computational grids is more preferable for solving the integral form of the NS equations than it would be on staggered grids. Considering the complexity of discretizing both integrals and derivatives, this gain is fundamental especially when the spatial discretization is performed at high accuracy order on a non-uniform grid, for example as done in Reference [5], or whereas unstructured grids have to be used. However, for long time, second-order discretizations on non-staggered grids have been considered inefficient in producing physically relevant solutions.

The main problem while using non-staggered grids can be addressed by these argumentations. On a side, if the discrete continuity equation has to be exactly satisfied, then the discrete pressure[‡] equation must be defined on a sparse stencil that, owing to the lack of communication between neighbouring nodes (odd–even decoupling), could produce unphysical oscillating solutions. On the other hand, if a compact stencil is used for obtaining a smooth pressure field, then the discrete continuity constraint is not satisfied up to machine-accuracy but it converges towards a source term that is proportional to fourth-order derivatives of the pressure field, multiplied by the time-step and the square of the grid step sizes [6–8]. Since projection methods are very popular [9–12], it is usual [13] to speak of *exact projection methods* (EPM) when the discrete continuity is exactly driven to zero whereas one speaks of *approximate projection methods* (APM) when the continuity is not zero at machine accuracy but converges towards the magnitude of the local truncation error. Despite the fact that both

---

[‡] The term ‘pressure equation’ will be used to indicate the elliptic equation that is solved to enforce continuity, though for the incompressible flow model there is no thermodynamic pressure equation but only a scalar field exists acting as a Lagrangian multiplier [1, 6].

formulations are consistent, in the first case one can get non-solenoidal modes, that can destroy the regularity of the solution, in the other case, for a finite grid measure, the mass source violates the discrete conservation of kinetic energy in the inviscid limit and this can be unacceptable, for example in simulating turbulence.

From a more rigorous mathematical point of view, one can distinguish between the EPM and APM formulations by looking at the Fourier symbol of the discrete Laplacian operators, e.g. see Reference [14]. One deduces that the nullspace of such operators has a dimension of eight (for 3D problems) in case of the EPM, whilst there is a dimension of one in the APM. Spurious zeros of the Fourier symbol in the EPM happens at the highest resolvable (Nyquist) frequencies, highlighting the existing grid decoupling in a checkerboard mode. Actually, since both EPM and APM formulations use, as a source term in Poisson equation, a discrete divergence operator on a large stencil, the nullspace of such operator has a dimension of eight and this fact can originate numerical oscillations in the APM, too.

Nevertheless, the continued advances in studies dedicated to these procedures allow us to use non-staggered grids for performing oscillation-free simulations of several flow problems but this goal still requires '*ad hoc*' cares, sometimes producing a degrading into the local accuracy of method. A strategy that has been successful for producing physical relevant solutions is based on a hybridization of the *traditional non-staggered grid*, in which all the variables are defined in the cell centres (Figure 1). A *hybrid non-staggered grid* is obtained while defining also the normal-to-face velocities in addition to the centred variables being such additional 'MAC-like staggered' variables obtainable by means of some suitable interpolation. Furthermore, a smoothing is obtained by adding '*ad hoc*' some dissipation terms [6, 15, 16] derived from suitable interpolations. This approach, which is called *momentum interpolation method* (MIM), has been successfully adopted for both steady and unsteady simulations [16] and extended to unstructured grids [17].

On the other hand, a special treatment of the pressure equation on uniform structured grid was instead proposed and analysed in Reference [8] while presenting both *single* and *two-steps* procedures. In the single-step procedure, a 19-points computational stencil was shown to be necessary for solving the pressure equation on a compact stencil (with no possible spurious modes) while modifying also the source term. However, apart from the consequent complications in the boundary conditions treatment, it was found that, owing to the enlargement of the bands of the matrix, the resulting computational procedure is very onerous being the number of iterations almost three times greater than that required by the classical 7-points scheme. Thus, in order to have a major computational efficiency, a two-steps procedure is proposed consisting in solving two consecutive elliptic equations having modified source terms but each one being discretized on a compact 7-points stencil. It was shown that these two elliptic solvers are more rapidly resolvable than the single one on the extended stencil. Such formulation still belongs to the class of APM formulation, the divergent constraint remaining only approximately ensured.

A further different remedy was proposed in Reference [14] wherein *projection filters* are designed to diffuse non-divergent modes that can be still present in the APM-based solution. The projection filter adopts only the main-diagonal part of the compact elliptic operator and the form of this projection mimics the Jacobian relaxation thus dumping high frequency errors. However, it is recognized that filters are equivalent to add finite difference expressions for dissipative-like derivatives (even derivatives) and some heuristic coefficients are introduced to modulate their impact on the solution. In fact, it was found that the solution quality degraded

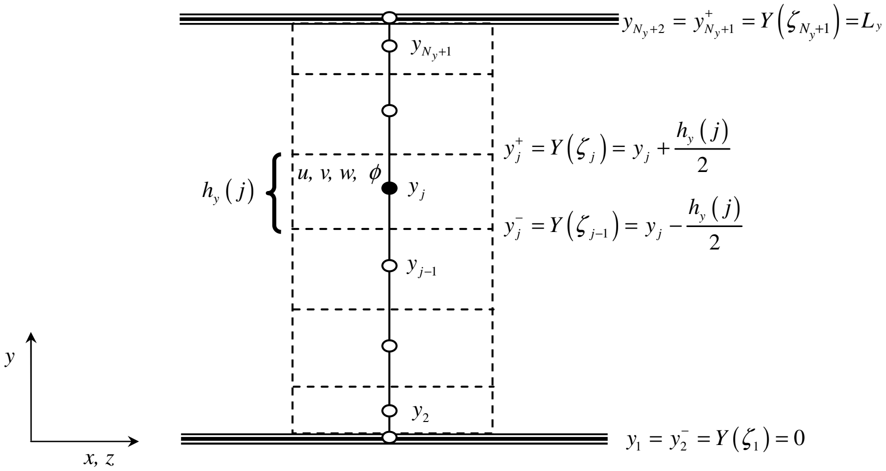

Traditional non-staggered grid

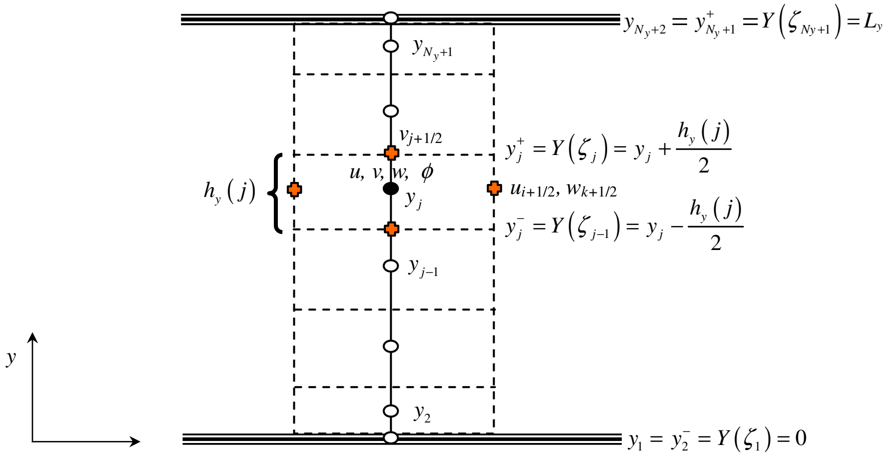

Hybrid non-staggered grid

Figure 1. Sketch of the adopted non-uniform, non-staggered structured grid. Traditional (upper) and hybrid (lower) non-staggered cell-centred collocation of the FV-based variables.

when such filters are applied in the entire flow field. Again, the discrete continuity is not exactly ensured.

How it appears from this framework, these strategies are generally based on the application of some sort of diffusion-like operators and it is an open discussion if they are suitable for simulating high Reynolds number flows, especially for simulating transitions towards turbulence as well as in cases in which turbulence is not in local equilibrium. Direct numerical simulation (DNS) and large eddy simulation (LES) are some of the most powerful methodologies for solving turbulent flows. In principle, the superimposed effect of diffusion-like operators appears less critical in DNS whereas the dissipative part of the real energy spectrum must be considered and it is numerically resolved. Conversely, the effect in LES appears much more critical since the MIM procedure or the diffusion-like operator-based strategies act on resolved wavenumbers corresponding to flow scales located close to the LES filter (very often it is also equivalent to the Nyquist grid cut-off). Therefore, the superimposed dissipation affects just those motion components in the inertial sub-range that are those then used in the turbulence model and consequently these strategies can dramatically alter the energy transfer. As a result, while dissipating high-frequencies errors mimics the similar physical behaviour of high wavenumbers flow components in DNS, the same is not true in LES and should be avoided. On the other hand, it is well known that the lack of mass conservation is a critical problem in turbulence since the kinetic energy (for incompressible flows it is only an induced quantity) results altered by an artificial contribution coming from the work done by the pressure (that is the term $p\underline{\nabla}\cdot\mathbf{v}$). Consequently, an APM formulation could be not well-suited for simulating turbulence.

Hence, after such picture, the spirit guiding this study can be expressed in these terms: to develop and test a non-diffusive methodology for exactly ensuring the continuity constraint in discrete sense while preventing the appearance of non-divergent modes. The projection-base FV method that is here proposed exploits the hybrid non-staggered grid in which both cell-centred and MAC-like staggered velocities are used. Anyway, it also uses the Helmholtz–Hodge decomposition (HHD) theorem [18] for deriving an additional potential velocity field (thus, without altering the vorticity field), defined only in a discrete sense, which enforces the discrete continuity to machine accuracy. This is accomplished by solving a first elliptic equation on a compact stencil, which appears in the same form of the APM formulation then, a second elliptic equation is obtained on a different stencil by prescribing that the additional discrete gradient ensures the continuity constraint in terms of a linear interpolation of the cell-centred velocities. Hence, while exploiting the hybrid non-staggered grid as in the MIM, this formulation can be seen in the framework of the two-steps procedures [8] and is thereafter addressed as *double projection method* (DPM). There is also a link between the DPM procedure and the projection filter one, which will be described in the following. Moreover, the convective fluxes are here discretized by means of a genuine second-order centred formula whereas in Reference [16] the intrinsically dissipative QUICK formula is used. Particularly, it is shown how to use the MAC-like, normal-to-face, divergence-free velocities computed after the first APM-based elliptic solver. The combination of sparse and non-sparse stencils as well as the use of centred and MAC-like velocities, allows a local grid coupling that, while ensuring the continuity constraint, stabilizes the solution without the need of adding *ad hoc* artificial viscosity.

In order for taking into account three-dimensional non-homogeneous flows, that is confined or interfacial flows, a specific attention is focused on the proper boundary conditions required by the DPM procedure. First, the new intermediate boundary conditions proposed in References [12, 18, 19] are exploited since, when the HHD is not orthogonal, not only the tangential intermediate velocity components but also the normal one must be properly prescribed on the boundaries otherwise the global accuracy of the method is affected. Then, it is illustrated how to prescribe the boundary conditions ensuring that the compatibility conditions are satisfied and a solution of the APM-based first elliptic step is obtainable. Furthermore, it is shown that prescribing boundary conditions consistently to those of the first elliptic equation allows us to satisfy the compatibility condition, ensuring the existence of a solution of the second elliptic equation. Hence, it is also illustrated how the DPM is implemented along the boundary of non-uniform structured grids. Extension to unstructured grids is therefore feasible as also briefly addressed in the paper.

The paper is subdivided in a first part, recalling the classical literature on the EPM and APM formulations, which illustrates the problems deriving from a second-order space–time discretization on 3D, non-uniform, non-staggered grid. Then the new DPM proposal is addressed and a paragraph is devoted to illustrate the main features in terms of stability and accuracy. Specifically, both a Neumann linear stability analysis and a convergence study on the vortex-decaying Taylor analytical solution are shown. Eventually, results of a buoyancy-driven flow at moderate Reynolds and Rayleigh number are illustrated in the last section. This flow resembles a simplified model of oceanographic flows [20] and is analysed as it has the critical task of reproducing a driving force that acts along the non-uniform direction as a normal stress. Therefore, this test appears appropriate since it is fundamental to obtain a good resolution of the pressure-like field as well as avoiding that erroneous compressibility effects alter the energy content of the motion. Besides, the absence of a mean shear flow allows us also to better analyse the presence of spurious oscillations and, since this is not a simply energy-decaying flow, one can experiment the superimposed effects due to the continuity error that could produce also a numerical instability during the evolution. The performances of two different discretizations of the convective terms, the first one corresponding to the adoption of a traditional non-staggered grid, the second one corresponding to the hybrid grid, are compared. The better property of the proposed DPM formulation is clearly shown since it guarantees an energy stable solution.

2. GOVERNING EQUATIONS AND DOMAIN DISCRETIZATION

The motion of incompressible Newtonian viscous flows in a domain V with regular boundaries, is governed by the momentum equation

$$\int_{\Omega(\mathbf{x})} \frac{\partial \mathbf{v}}{\partial t}\,\mathrm{d}V + \int_{\partial\Omega(\mathbf{x})} \mathbf{n}\cdot(\mathbf{v}\mathbf{v})\,\mathrm{d}S + \int_{\partial\Omega(\mathbf{x})} \mathbf{n}p'\,\mathrm{d}S = \int_{\partial\Omega(\mathbf{x})} \mathbf{n}\cdot(2\nu\mathbf{D})\,\mathrm{d}S \tag{1}$$

here written in integral form over a finite volume $\Omega(\mathbf{x}) \subseteq V$ with boundary $\partial\Omega$ and its outward-oriented normal unit vector $\mathbf{n}$, being $\mathbf{D} = \underline{\nabla}^s\mathbf{v}$ the symmetric velocity gradient having zero trace (constraint (2) allows to get $\int_{\partial\Omega} \mathbf{n}\cdot(2\nu\mathbf{D})\,\mathrm{d}S = \int_{\partial\Omega} \mathbf{n}\cdot(\nu\nabla^{\mathrm{T}}\mathbf{v})\,\mathrm{d}S$), ν is the kinematics viscosity and $p' = p/\rho_0$ with p the static pressure. For incompressible fluid it is well known that, owing to the continuity constraint

$$\int_{\partial\Omega(\mathbf{x})} \mathbf{n}\cdot\mathbf{v}\,\mathrm{d}S = 0 \tag{2}$$

that must be ensured everywhere and for all time, the pressure is only a Lagrangian multiplier. In order to close the mathematical problem constituted by Equations (1) and (2), proper initial and boundary conditions are prescribed over the frontier ∂V, e.g. see Reference [1].

In case of buoyancy-driven flows, the hypothesis of incompressibility remains valid, the density depends only on small temperature gradients and the coupling between the internal energy and the momentum quantity being prescribed by means of the Bousinnesq model. For the sake of simplicity, this coupling is not considered in the following discussions since it does not add an issue to the key-point concerning the imposition of the continuity constraint. Moreover, the complete set of governing equations will be shown in Section 7.

The computational domain $V = [0, L_x] \times [0, L_y] \times [0, L_z]$ is partitioned by means of a Cartesian structured grid. Along the x- and z-flow directions, assumed to be homogeneous, the FV centres are uniformly distributed according to

$$\begin{aligned} x_i &= (i - \tfrac{1}{2})\Delta x, \quad (i = 2, \ldots, N_x + 1) \\ z_k &= (k - \tfrac{1}{2})\Delta z, \quad (k = 2, \ldots, N_z + 1) \end{aligned} \tag{3}$$

being $\Delta x = L_x/N_x$, $\Delta z = L_z/N_z$ the step sizes and N_x, N_z the number of FVs in these directions.

Along the y-direction, assumed to be non-homogeneous, a non-uniform grid is introduced by means of a 1-D mapping $y = Y(\zeta)$, ζ being the independent variable in the transformed axis. The latter is uniformly partitioned in $N_y + 1$ nodes according to $\zeta_p = (p-1)h$, $(p = 1, \ldots, N_y + 1)$, $h = L_y/N_y$ being the grid-spacing and N_y the number of subdivisions in ζ-direction. Thus, the FV face co-ordinates in the physical space (see Figure 1) are defined by $y_j^- = Y(\zeta_{j-1})$ and $y_j^+ = Y(\zeta_j)$, $(j = 2, \ldots, N_y + 1)$ and, subsequently, the N_y FV centres are suitably located at the cell barycentre as

$$y_j = (y_j^- + y_j^+)/2, \quad (j = 2, \ldots, N_y + 1) \tag{4}$$

Fixing the boundaries nodes $y_1 = y_2^- = 0$, $y_{N_y+2} = y_{N_y+1}^+ = L_y$ completes the domain partition. Moreover, the distance between two adjacent FV centres is defined as $\Delta y_j \equiv y_j - y_{j-1} = (y_j^+ - y_{j-1}^-)/2$, while the FV width along the y-direction is

$$h_y(j) = y_j^+ - y_j^- = Y(\zeta_{j+1}) - Y(\zeta_j) = hY'(\zeta_j) + h^2 Y''(\zeta_j)/2 + \cdots \tag{5}$$

Let us note that a smooth mapping will be assumed (i.e. a cosine law), so that $h_y/h = O(1)$.

Finally, one has the FV definition $\Omega(x_i, y_j, z_k) \equiv \Omega_{ijk} = [x_i^-, x_i^+] \times [y_j^-, y_j^+] \times [z_k^-, z_k^+]$, $|\Omega_{ijk}| = \Delta x h_y(j) \Delta z$, where the face co-ordinates can be expressed in terms of the cell centre co-ordinates as

$$\begin{aligned} x_i^- &= x_i - \Delta x/2, \quad x_i^+ = x_i + \Delta x/2 \\ y_j^- &= y_j - h_y(j)/2, \quad y_j^+ = y_j + h_y(j)/2 \\ z_k^- &= z_k - \Delta z/2, \quad z_k^+ = z_k + \Delta z/2 \end{aligned} \tag{6}$$

This way, the frontier ∂V is discretized by a set of FV flux-sections $\{\partial\Omega\}$. Henceforth, the explicit dependence of h_y from j is omitted and, whereas possible, the simplified index notation $x_i^{\pm} = i \pm 1/2$, $y_j^{\pm} = j \pm 1/2$, $z_k^{\pm} = k \pm 1/2$ is used for defining the faces co-ordinates. As shown in Figure 1, all the unknown flow quantities are co-located in the FV centre (i, j, k) defined by Equations (3), (4) constituting the framework of the traditional non-staggered grid.

3. TIME INTEGRATION

The time integration of the momentum equation (1) is based on the second-order accurate semi-implicit Adams–Bashforth/Crank–Nicolson (AB/CN) scheme. In particular, only the diffusive terms along the y-axis are integrated according to the CN approximation, while the AB time-extrapolation is adopted for all the others. According to such integration method, since for cell-centred velocities the second-order approximation $\mathbf{v} \cong \overline{\mathbf{v}}$ (the bar indicating a volume average over Ω) applies, the discrete momentum equation written in a generic position (i, j, k), along with the associated boundary conditions, becomes

$$\begin{aligned}\left(I - \frac{\nu\Delta t}{2} D_2\right)\mathbf{v}^{n+1} &= \left(I + \frac{\nu\Delta t}{2} D_2\right)\mathbf{v}^n + \int_{t^n}^{t^{n+1}} \mathbf{m}_{\text{press}}\,\mathrm{d}t \\ &\quad + \frac{\Delta t}{2}\{3[\nu(D_1 + D_3)\mathbf{v}^n + \mathbf{m}^n_{\text{conv}}] - [\nu(D_1 + D_3)\mathbf{v}^{n-1} + \mathbf{m}^{n-1}_{\text{conv}}]\} \\ \mathbf{v}^{n+1} &= \mathbf{v}_b^{n+1} \quad \text{on } \partial V\end{aligned} \tag{7}$$

having defined the identity operator I, the vector fields

$$\mathbf{m}_{\text{conv}} = -\frac{1}{|\Omega(\mathbf{x})|}\int_{\partial\Omega(\mathbf{x})} (\mathbf{v}\mathbf{v})\cdot\mathbf{n}\,\mathrm{d}S, \quad \mathbf{m}_{\text{pres}} = -\frac{1}{|\Omega(\mathbf{x})|}\int_{\partial\Omega(\mathbf{x})} p'\mathbf{n}\,\mathrm{d}S \tag{8}$$

and the integro-differential operators acting along the Cartesian directions as D_1, D_2, D_3

$$\begin{aligned} D_1() &\equiv \frac{1}{|\Omega(\mathbf{x})|}\int_{z^-}^{z^+} \mathrm{d}\zeta \int_{y^-}^{y^+} \left(\left.\frac{\partial}{\partial\xi}\right|_{x^+} - \left.\frac{\partial}{\partial\xi}\right|_{x^-}\right)\mathrm{d}\eta \\ D_2() &\equiv \frac{1}{|\Omega(\mathbf{x})|}\int_{z^-}^{z^+} \mathrm{d}\zeta \int_{x^-}^{x^+} \left(\left.\frac{\partial}{\partial\eta}\right|_{y^+} - \left.\frac{\partial}{\partial\eta}\right|_{y^-}\right)\mathrm{d}\xi \\ D_3() &\equiv \frac{1}{|\Omega(\mathbf{x})|}\int_{y^-}^{y^+} \mathrm{d}\eta \int_{x^-}^{x^+} \left(\left.\frac{\partial}{\partial\zeta}\right|_{z^+} - \left.\frac{\partial}{\partial\zeta}\right|_{z^-}\right)\mathrm{d}\xi \end{aligned} \tag{9}$$

$x^\pm, y^\pm$ and $z^\pm$ being the FV face co-ordinates as defined in (6).

The velocity-pressure de-coupling is obtained by means of the *pressure-free projection method* [9–12], which is based on a prediction step, wherein a non-solenoidal vector field $\mathbf{v}^*$ is obtained by solving Equation (7) without considering the pressure term,

$$\begin{aligned}\left(I - \frac{\nu\Delta t}{2} D_2\right)\mathbf{v}^* &= \left(I + \frac{\nu\Delta t}{2} D_2\right)\mathbf{v}^n + \frac{\Delta t}{2}\{3[\nu(D_1 + D_3)\mathbf{v}^n + \mathbf{m}^n_{\text{conv}}] \\ &\quad - [\nu(D_1 + D_3)\mathbf{v}^{n-1} + \mathbf{m}^{n-1}_{\text{conv}}]\} \\ \mathbf{v}^* &= \mathbf{v}_b^* \text{ on } \partial V\end{aligned} \tag{10}$$

along with proper intermediate boundary conditions, here assigned following a new procedure reported in References [12, 18, 19]. It is worthwhile remarking that, in (10), the discrete velocities fields $\mathbf{v}^n$, $\mathbf{v}^{n-1}$ must be divergence-free.

Again, the buoyancy term can be easily added in the discrete equation (10) since the integral of the temperature can be approximated by means of either the CN or AB schemes. In fact, Equation (10) represents also the adopted time-discretization for the advection–diffusion temperature equation shown later in Section 6. Therefore, even if the momentum equation is coupled with the temperature one, this latter can be updated without having to compute before the field $\mathbf{v}^*$.

Eventually, assume that a second-order centred spatial discretization[§] of (10) has been performed and thus allowed us to compute the discrete intermediate velocity. That is, a set of discrete values, let say $\{u^*, v^*, w^*\}_C$ is available in the centres of the previously defined FVs. Then, in order to obtain a final vector field $\mathbf{v}^{n+1}$, the intermediate velocity is projected into the sub-space of the divergence-free vector fields. Indeed, according to the Helmholtz–Hodge decomposition, $\mathbf{v}^*$ is expressed as the sum of the divergence-free velocity field $\mathbf{v}^{n+1}$ and a pure gradient field

$$\mathbf{v}^{n+1} = \mathbf{v}^* - \Delta t \underline{\nabla} \phi^{n+1} \tag{11}$$

Decomposition (11) applies both in continuous and discrete sense. However, it is well known that, after time discretization, $\underline{\nabla}\phi$ will be only a first-order (in time) approximation of the real pressure gradient although this does not affect the velocity accuracy provided that the decomposition (11) is really orthogonal [9–12, 18, 19]. Now, the setting of the projection step on non-staggered grid is illustrated.

4. SETTING AND DISCRETIZATION OF THE PRESSURE PROBLEM: THE APM STEP

The guidelines of the procedure, developed on non-uniform, non-staggered grids, are now highlighted along with the resulting key-problem. Although some of the main aspects are well recognized in the literature, for the sake of completeness and before presenting the new ideas, the issue is illustrated.

Starting from the HHD, by taking the divergence of both sides of (11) and integrating over a generic FV, after applying the Gauss theorem and setting the updated velocity field to be divergence-free, one gets the equation

$$\frac{1}{|\Omega|}\int_{\partial\Omega} \mathbf{n}\cdot\mathbf{v}^{n+1}\,\mathrm{d}S = 0 = \frac{1}{|\Omega|}\int_{\partial\Omega} \mathbf{n}\cdot\mathbf{v}^{*}\,\mathrm{d}S - \Delta t\frac{1}{|\Omega|}\int_{\partial\Omega} \mathbf{n}\cdot\underline{\nabla}\phi^{n+1}\,\mathrm{d}S \tag{12}$$

that has to be discretized while collocating the variables in the FV centres, see (3), (4). Let us highlight that, at this stage of the projection procedure, the discrete set $\{u^*, v^*, w^*\}_C$ is the only already available and represents the source term in (12), the final goal being to obtain the divergence-free velocity in the centres of the FVs, i.e. a set of discrete values, let say $\{u^{n+1}, v^{n+1}, w^{n+1}\}_C$.

Owing to the adopted grid system, a second-order discretization of the surface integral can be obtained by exploiting the simple mean value formula. This means that a surface integral

---

[§] Let us recall that the momentum interpolation method proposed in Reference [16] exploits the upwinded QUICK discretization for the convective terms. Actually, in this study, a genuine second-order centred discretization is used in two different forms as detailed in Section 7.

of a generic vector field $\mathbf{f} \equiv (fx, fy, fz)$ can be approximated as

$$
\begin{aligned}
\frac{1}{|\Omega_{ijk}|}\int_{\partial\Omega_{ijk}} \mathbf{n}\cdot\mathbf{f}\,\mathrm{d}S = \frac{1}{\Delta x h_y \Delta z}\Bigg[&\int_{z_k^-}^{z_k^+}\mathrm{d}z\int_{y_j^-}^{y_j^+}(fx|_{x_i^+} - fx|_{x_i^-})\,\mathrm{d}y \\
&+\int_{z_k^-}^{z_k^+}\mathrm{d}z\int_{x_i^-}^{x_i^+}(fy|_{y_j^+} - fy|_{y_j^-})\,\mathrm{d}x + \int_{x_i^-}^{x_i^+}\mathrm{d}x\int_{y_j^-}^{y_j^+}(fz|_{z_k}^{+} - fz|_{z_k^-})\,\mathrm{d}y\Bigg] \\
\cong\ & \frac{(fx|_{i+1/2,j,k} - fx|_{i-1/2,j,k})}{\Delta x} + \frac{(fy|_{i,j+1/2,k} - fy|_{i,j-1/2,k})}{h_y} \\
&+ \frac{(fz|_{i,j,k+1/2} - fz|_{i,j,k-1/2})}{\Delta z}
\end{aligned}
\tag{13}
$$

Observe that (13) would be practically computable provided that the face-centred values are available, as happens in the staggered MAC method. Thus, if the generic components (fx, fy, fz) correspond to partial derivatives along x, y and z directions, respectively, then it is rather natural to rewrite (13) only in terms of cell-centred values, while exploiting a second-order FD approximation for each derivative. On the other hand, whereas the components (fx, fy, fz) would correspond to the normal-to-face velocity components then it seems suitable to adopt a local linear interpolation and expanding (13) in terms of the cell-centre values. At the present stage, one could suppose that the linear interpolation of the velocities would maintain the desired second-order accuracy. Actually, accuracy is not all is required to get physically relevant solutions on non-staggered grids. This issue is the key-point; it will be developed in the next section wherein the resulting local truncation error in the mass equation will be analysed.

According to such observations, the two integrals in the RHS of (12) can be simply approximated as

$$
\begin{aligned}
\frac{1}{|\Omega_{ijk}|}\int_{\partial\Omega_{ijk}} \mathbf{n}\cdot\mathbf{v}^*\,\mathrm{d}S \cong\ & \frac{u^*_{i+1/2,j,k} - u^*_{i-1/2,j,k}}{\Delta x} \\
&+ \frac{v^*_{i,j+1/2,k} - v^*_{i,j-1/2,k}}{h_y} + \frac{w^*_{i,j,k+1/2} - w^*_{i,j,k-1/2}}{\Delta z} \\
\cong\ & \frac{1}{\Delta x}\left(\frac{u^*_{i+1,j,k} + u^*_{i,j,k}}{2} - \frac{u^*_{i,j,k} + u^*_{i-1,j,k}}{2}\right) \\
&+ \frac{1}{h_y}(N^{\mathrm{nord}}_{j+1} v^*_{i,j+1,k} + N^{\mathrm{nord}}_{j} v^*_{i,j,k} - N^{\mathrm{sud}}_{j} v^*_{i,j,k} - N^{\mathrm{sud}}_{j-1} v^*_{i,j-1,k}) \\
&+ \frac{1}{\Delta z}\left(\frac{w^*_{i,j,k+1} + w^*_{i,j,k}}{2} - \frac{w^*_{i,j,k} + w^*_{i,j,k-1}}{2}\right)
\end{aligned}
\tag{14}
$$

and

$$
\begin{aligned}
\frac{1}{|\Omega_{ijk}|}\int_{\partial\Omega_{ijk}} \mathbf{n}\cdot\underline{\nabla}\phi^{n+1}\,\mathrm{d}S &\cong \frac{\phi_x|^{n+1}_{i+1/2,j,k}-\phi_x|^{n+1}_{i-1/2,j,k}}{\Delta x}\\
&\quad+\frac{\phi_y|^{n+1}_{i,j+1/2,k}-\phi_y|^{n+1}_{i,j-1/2,k}}{h_y}+\frac{\phi_z|^{n+1}_{i,j,k+1/2}-\phi_z|^{n+1}_{i,j,k-1/2}}{\Delta z}\\
&\cong \frac{1}{\Delta x}\left(\frac{\phi^{n+1}_{i+1,j,k}-\phi^{n+1}_{i,j,k}}{\Delta x}-\frac{\phi^{n+1}_{i,j,k}-\phi^{n+1}_{i-1,j,k}}{\Delta x}\right)\\
&\quad+\frac{1}{h_y}\left(\frac{\phi^{n+1}_{i,j+1,k}-\phi^{n+1}_{i,j,k}}{y_{j+1}-y_j}-\frac{\phi^{n+1}_{i,j,k}-\phi^{n+1}_{i,j-1,k}}{y_j-y_{j-1}}\right)\\
&\quad+\frac{1}{\Delta z}\left(\frac{\phi^{n+1}_{i,j,k+1}-\phi^{n+1}_{i,j,k}}{\Delta z}-\frac{\phi^{n+1}_{i,j,k}-\phi^{n+1}_{i,j,k-1}}{\Delta z}\right)
\end{aligned}
\tag{15}
$$

having defined the linear shape functions along the non-uniform direction according to

$$
\begin{aligned}
N^{\text{nord}}_{j+1}&=\frac{y^+_j-y_j}{y_{j+1}-y_j}=\frac{h_y}{2\Delta y_{j+1}}, \quad N^{\text{nord}}_{j}=\frac{y_{j+1}-y^+_j}{y_{j+1}-y_j}=1-\frac{h_y}{2\Delta y_{j+1}}\\
N^{\text{sud}}_{j}&=\frac{y^-_j-y_{j-1}}{y_j-y_{j-1}}=1-\frac{h_y}{2\Delta y_j}, \quad N^{\text{sud}}_{j-1}=\frac{y_j-y^-_j}{y_j-y_{j-1}}=\frac{h_y}{2\Delta y_j}
\end{aligned}
\tag{16}
$$

being $N^{\text{nord}}_j-N^{\text{sud}}_j=h_y(\Delta y_{j+1}-\Delta y_j)/(2\Delta y_j\Delta y_{j+1})$.

It follows that, by substituting (14) and (15) into Equation (12), one gets the second-order accurate discrete pressure equation

$$
\begin{aligned}
&-\phi^{n+1}_{i,j,k}\left[\frac{2}{\Delta x^2}+\frac{2}{\Delta z^2}+\frac{1}{h_y}\left(\frac{1}{\Delta y_{j+1}}+\frac{1}{\Delta y_j}\right)\right]+\frac{\phi^{n+1}_{i+1,j,k}+\phi^{n+1}_{i-1,j,k}}{\Delta x^2}\\
&\quad+\frac{\phi^{n+1}_{i,j,k+1}+\phi^{n+1}_{i,j,k-1}}{\Delta z^2}+\frac{\phi^{n+1}_{i,j+1,k}}{h_y\Delta y_{j+1}}+\frac{\phi^{n+1}_{i,j-1,k}}{h_y\Delta y_j}=\frac{1}{\Delta t}\left[\frac{u^*_{i+1,j,k}-u^*_{i-1,j,k}}{2\Delta x}\right.\\
&\quad\left.+\frac{N^{\text{nord}}_{j+1}v^*_{i,j+1,k}+(N^{\text{nord}}_j-N^{\text{sud}}_j)v^*_{i,j,k}-N^{\text{sud}}_{j-1}v^*_{i,j-1,k}}{h_y}+\frac{w^*_{i,j,k+1}-w^*_{i,j,k-1}}{2\Delta z}\right]
\end{aligned}
\tag{17}
$$

defined on a compact stencil for the discrete Laplacian operator [6–8, 13–18] which guarantees a strong coupling between its neighbouring nodes. This represents the APM-based pressure equation.

Clearly, on non-staggered grids, the *normal-to-face intermediate velocities*, that would correspond to three sets of grid-staggered velocities, let say $\{u^*\}_f, \{v^*\}_f, \{w^*\}_f$, are not directly available after having solved Equation (10) as happens instead in the MAC method.

Hence, one can consider an existing functional approximation between the staggered MAC-like sets $\{u^*\}_f, \{v^*\}_f, \{w^*\}_f$ and the non-staggered set $\{u^*, v^*, w^*\}_C$ that, according to the global second-order approximation of the method, is symbolically represented by $\{u^*\}_f, \{v^*\}_f, \{w^*\}_f = N[\{u^*, v^*, w^*\}_C]$, N indicating the linear interpolation operator. Thus, if one thinks of the resulting pressure equation in the original staggered MAC method, it appears that (17) differs only in the source term. One can easily see that the discrete source term is based on a large stencil, therefore spurious modes can appear at high wavenumbers.

Conversely, a different approach that would allow us to use directly the non-staggered set $\{u^*, v^*, w^*\}_C$, assuming them as normal-to-face velocities, would involve a wider stencil for discrete Laplacian operator and the consequent appearing of odd–even decoupling. These issues address the main difference existing between the APM and EPM formulations. It is well known [9, 13, 14] that the EPM formulation suffers by the fact that the nullspace of the discrete Laplacian operator has a dimension of eight (for 3D problems) whilst there is a dimension of one in that used in the APM. Spurious zeros of the Fourier symbol in the EPM appears at the highest resolvable (i.e. Nyquist) frequencies highlighting the existing neighbouring grid decoupling. This fact can produce numerical oscillations that can amplify and destroy the stability of the computation therefore the EPM is not here considered.

In the present study, the boundary conditions to be associated to Equation (17) prescribe the periodicity along the x and z directions while, along the non-homogeneous vertical direction y, one must prescribe that the pressure gradient allows the correct flow rate through the surfaces. Furthermore, the compatibility conditions ensuring the existence of a solution (apart a constant) must be fulfilled. Hence, the non-homogeneous Neumann condition

$$\left.\frac{\partial \phi}{\partial y}\right|_{i, j_{\text{bnd}}, k}^{n+1} = \frac{1}{\Delta t}(v^*_{i, j_{\text{bnd}}, k} - v^{n+1}_{i, j_{\text{bnd}}, k}) \tag{18}$$

is prescribed, $v^{n+1}_{i, j_{\text{bnd}}, k}$ being a known value and (see Figure 1) $j_{\text{bnd}} = 1$ or $j_{\text{bnd}} = N_y + 2 \equiv m$.

As a practical example, if one considers the upper frontier (see Figure 2) located at $j_{\text{bnd}} = m$, then Equation (17) is rewritten for each node having $\bar{j} = m - 1$ (and for nodes not involving periodic boundary conditions) in the following way.

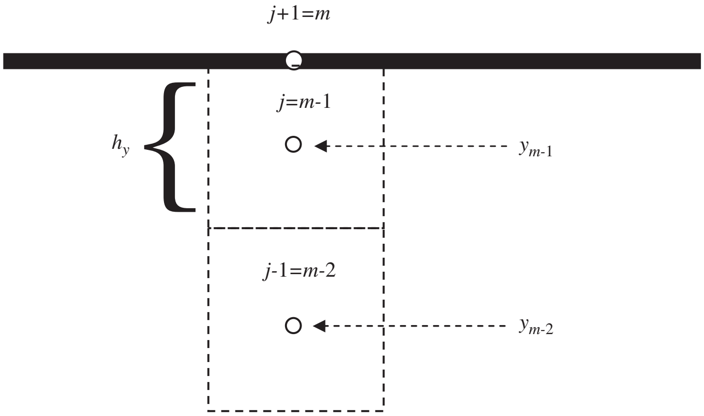

Figure 2. Sketch of the stencil where boundary conditions for the pressure equation are prescribed.

By exploiting condition (18), since $\phi_y|^{n+1}_{i,\bar{j}+1/2,k} = \phi_y|^{n+1}_{i,m,k}$, one gets

$$\frac{\phi_y|^{n+1}_{i,\bar{j}+1/2,k} - \phi_y|^{n+1}_{i,\bar{j}-1/2,k}}{h_y} = \frac{1}{h_y}\left(\frac{v^*_{i,m,k} - v^{n+1}_{i,m,k}}{\Delta t} - \phi_y|^{n+1}_{i,m-3/2,k}\right) \tag{19}$$

then, observing that $N^{\text{nord}}_m = h_y/2\Delta y_m = 1, N^{\text{nord}}_{m-1} = 1 - h_y/2\Delta y_m = 0$ (see Figure 2), one gets also

$$\frac{v^*_{i,\bar{j}+1/2,k} - v^*_{i,\bar{j}-1/2,k}}{h_y\Delta t} = \frac{v^*_{i,m,k} - N^{\text{sud}}_{m-1} v^*_{i,m-1,k} - N^{\text{sud}}_{m-2} v^*_{i,m-2,k}}{h_y\Delta t} \tag{20}$$

Therefore, combining (19) and (20), one rewrites Equation (17) at $\bar{j}$ while including the boundary condition (18), according to

$$\begin{aligned} -\phi^{n+1}_{i,m-1,k}\left(\frac{2}{\Delta x^2} + \frac{2}{\Delta z^2} + \frac{1}{h_y \Delta y_{m-1}}\right) + \frac{\phi^{n+1}_{i+1,m-1,k} + \phi^{n+1}_{i-1,m-1,k}}{\Delta x^2} \\ + \frac{\phi^{n+1}_{i,m-1,k+1} + \phi^{n+1}_{i,m-1,k-1}}{\Delta z^2} + \frac{\phi^{n+1}_{i,m-2,k}}{h_y \Delta y_{m-1}} = \frac{u^*_{i+1,m-1,k} - u^*_{i-1,m-1,k}}{2\Delta t \Delta x} \\ + \frac{w^*_{i,m-1,k+1} - w^*_{i,m-1,k-1}}{2\Delta t \Delta z} + \frac{v^{n+1}_{i,m,k} - N^{\text{sud}}_{m-1} v^*_{i,m-1,k} - N^{\text{sud}}_{m-2} v^*_{i,m-2,k}}{h_y \Delta t} \end{aligned} \tag{21}$$

It is important to remark how the implementation of the boundary condition (18) has involved only variables located at computational nodes, no interpolation or extra-points being required. Besides, it is not necessary to perform any discretization¶ in (18), only a simple substitution of (19) and (20) in (14) and (15) eliminates the need of prescribing the gradient as well as the intermediate field on the frontier. The unique requirement remains to prescribe the correct values of the normal velocity. The resulting Poisson problem becomes equivalent to the one with homogeneous Neumann boundary conditions and a modified source term, e.g. see Reference [18].

The implementation of the boundary conditions along the directions of periodicity, is performed by linking the values at $i=1$ with those at $i=N_x$ and the values at $i=N_x+2$ with those at $i=2$ and rewriting suitably Equation (21). Analogously one proceeds for the direction k.

This way, the discrete counterpart of the compatibility condition is verified and a solution of the pressure problem is ensured.

5. DEFINITION OF THE CORRECTION STEP

Once that the pressure problem has been solved, one possesses the collocated set $\{u^*, v^*, w^*, \phi^{n+1}\}_C$. Hence, in order for the procedure to be completed, one must derive form it the set

---

¶ A discretization of the pressure gradient on the boundary, is required only for assigning time-accurate intermediate boundary conditions, see Reference [19].

of updated discrete velocity field, let say $\{u^{n+1}, v^{n+1}, w^{n+1}\}_C$, that is collocated in the same nodes of the previously computed set. The discretization of the decomposition (11) represents what is here called the *correction step* that is the final step of the fractional procedure. Of course, the resulting vector field $\mathbf{v}^{n+1}$ must result divergence-free in a discrete sense namely, it is expected that, while exploiting the set $\{u^{n+1}, v^{n+1}, w^{n+1}\}_C$, the discrete continuity constraint (12) applies in each FV.

This is the key-point of the procedure. Indeed, even though the APM-based Laplacian operator has been discretized on a compact stencil, the fulfilment of the continuity constraint in terms of the set $\{u^{n+1}, v^{n+1}, w^{n+1}\}_C$ is not ensured, as on the contrary happens in the original MAC method, but it depends on the correction step. Let us clarify this issue.

Remember that, in deriving the pressure equation (17), the following discrete continuity constraint, see (12) and (13),

$$\frac{1}{|\Omega_{ijk}|}\int_{\partial\Omega_{ijk}} \mathbf{n}\cdot\mathbf{v}^{n+1}\,\mathrm{d}S \cong \frac{(u^{n+1}_{i+1/2,j,k} - u^{n+1}_{i-1/2,j,k})}{\Delta x} + \frac{(v^{n+1}_{i,j+1/2,k} - v^{n+1}_{i,j-1/2,k})}{h_y} + \frac{(w^{n+1}_{i,j,k+1/2} - w^{n+1}_{i,j,k-1/2})}{\Delta z} = 0 \tag{22}$$

has been imposed for each FV. Actually, Equation (22) appears in the (staggered) MAC-like form that is the discrete constraint applies in terms of the sets of *normal-to-face updated velocities*, let say $\{u^{n+1}\}_f, \{v^{n+1}\}_f, \{w^{n+1}\}_f$, not involving at all the updated velocity values in the FV centres (collocated). Thus, at this stage, it is clear that only the staggered sets ensure that (22) is fulfilled. In the following, constraint (22) will be also symbolically expressed by means of such sets as $D[\{u^{n+1}\}_f, \{v^{n+1}\}_f, \{w^{n+1}\}_f] = 0$.

On the other hand, these updated staggered velocities can be computed by writing the decomposition (11) in its scalar components while properly discretizing them at a second-order accuracy. This is obtained by exploiting the staggered intermediate velocities, i.e. $\{u^*\}_f, \{v^*\}_f, \{w^*\}_f = N[\{u^*, v^*, w^*\}_C]$, defined in the previous section, along with centred FD derivatives expressed in terms of $\{\phi^{n+1}\}_C$. Hence, in each FV, one writes the discrete MAC-like components of (11) according to

$$\begin{aligned}
u^{n+1}_{i\pm1/2,j,k} &\cong \frac{u^*_{i\pm1,j,k} + u^*_{i,j,k}}{2} \mp \Delta t\left(\frac{\phi^{n+1}_{i\pm1,j,k} - \phi^{n+1}_{i,j,k}}{\Delta x}\right)\\
v^{n+1}_{i,j+1/2,k} &\cong (N^{\text{nord}}_{j+1} v^*_{i,j+1,k} + N^{\text{nord}}_{j} v^*_{i,j,k}) - \Delta t\left(\frac{\phi^{n+1}_{i,j+1,k} - \phi^{n+1}_{i,j,k}}{y_{j+1} - y_j}\right)\\
v^{n+1}_{i,j-1/2,k} &\cong (N^{\text{sud}}_{j} v^*_{i,j,k} + N^{\text{sud}}_{j-1} v^*_{i,j-1,k}) - \Delta t\left(\frac{\phi^{n+1}_{i,j,k} - \phi^{n+1}_{i,j-1,k}}{y_j - y_{j-1}}\right)\\
w^{n+1}_{i,j,k\pm1/2} &\cong \frac{w^*_{i,j,k\pm1} + w^*_{i,j,k}}{2} \mp \Delta t\left(\frac{\phi^{n+1}_{i,j,k\pm1} - \phi^{n+1}_{i,j,k}}{\Delta z}\right)
\end{aligned} \tag{23}$$

For the sake of brevity, hereafter, the Equations (23) will be also symbolically expressed as a linear functional relation between the MAC-like sets $\{u^{n+1}\}_f, \{v^{n+1}\}_f, \{w^{n+1}\}_f$ and the collocated set $\{u^*, v^*, w^*, \phi^{n+1}\}_C$, according to

$$\{u^{n+1}\}_f, \{v^{n+1}\}_f, \{w^{n+1}\}_f = N[\{u^*, v^*, w^*\}_C] - G[\{\phi^{n+1}\}_C]$$

$G[\{\phi^{n+1}\}_C]$ symbolically expressing the discrete gradient on a compact (again MAC-like) stencil. Hence, it can be easily shown that, by substituting the Equations (23) in (22), the pressure equation (17) is exactly recovered and therefore it is demonstrated that the discrete continuity constraint $D[\{u^{n+1}\}_f, \{v^{n+1}\}_f, \{w^{n+1}\}_f] = 0$ is fulfilled.

The evident trouble is that, up to now, one has no clear information on how to compute the set $\{u^{n+1}, v^{n+1}, w^{n+1}\}_C$ that simultaneously satisfies, in discrete sense, the continuity constraint while according to the decomposition (11), the only sureness is that the MAC-like velocity update (23) is divergence-free. As a consequence, any way to produce an expression for getting $\{u^{n+1}, v^{n+1}, w^{n+1}\}_C$, will correspond to the assumption of existence of some functional relation, let say F, between the collocated and staggered updated velocity sets, that is

$$\begin{aligned}\{u^{n+1}, v^{n+1}, w^{n+1}\}_C &= F[\{u^{n+1}\}_f, \{v^{n+1}\}_f, \{w^{n+1}\}_f]\\ &= F[N[\{u^*, v^*, w^*\}_C] - G[\{\phi^{n+1}\}_C]]\end{aligned}$$

On the other hand, since $D[\{u^{n+1}\}_f, \{v^{n+1}\}_f, \{w^{n+1}\}_f] = 0$, the above functional relation should simultaneously ensure that $D[F^{-1}[\{u^{n+1}, v^{n+1}, w^{n+1}\}_C]] = 0$, denoting with F^{-1} an implicit inverse operator. Actually, there is no guarantee that an arbitrary functional relation F will allow us to satisfy this constraint. Let us now analyse some of the possible choices for F, the first one being the most straightforward correction that does not exactly ensure mass conservation, the other one being the new proposal presented in this study.

5.1. The APM framework: first-order in time accurate correction step

In order for the velocity values in the FV centres to be updated, one could perform the correction step exploiting exclusively the available set $\{u^*, v^*, w^*, \phi^{n+1}\}_C$. In fact, the decomposition (11) can be discretized in the cell-centred nodes at second accuracy according to

$$\begin{aligned}u^{n+1}_{i,j,k} &= u^*_{i,j,k} - \Delta t\left(\frac{\phi^{n+1}_{i+1,j,k} - \phi^{n+1}_{i-1,j,k}}{2\Delta x}\right)\\ v^{n+1}_{i,j,k} &= v^*_{i,j,k} - \Delta t\left(\frac{\phi^{n+1}_{i,j+1,k} - \phi^{n+1}_{i,j-1,k}}{y_{j+1} - y_{j-1}}\right)\\ w^{n+1}_{i,j,k} &= w^*_{i,j,k} - \Delta t\left(\frac{\phi^{n+1}_{i,j,k+1} - \phi^{n+1}_{i,j,k-1}}{2\Delta z}\right)\end{aligned} \qquad (24)$$

These expressions, can be symbolically indicated as $\{u^{n+1}, v^{n+1}, w^{n+1}\}_C = \{u^*, v^*, w^*\}_C - G_c[\{\phi^{n+1}\}_C]$, $G_c[\{\phi^{n+1}\}_C]$ expressing now the discrete gradient on the large stencil (rigorously speaking, $G_c[\{\phi^{n+1}\}_C]$ implies three discrete components whereas $G[\{\phi^{n+1}\}_C]$ indicated the six ones in (23)). As before addressed, expressions (24) imply to have intrinsically specified a functional relation between the collocated and the staggered sets, in fact, one can write

$$\begin{aligned}\{u^{n+1}, v^{n+1}, w^{n+1}\}_C &= \{u^*, v^*, w^*\}_C - G_c[\{\phi^{n+1}\}_C]\\ &= F[\{u^{n+1}\}_f, \{v^{n+1}\}_f, \{w^{n+1}\}_f] = F[N[\{u^*, v^*, w^*\}_C] - G[\{\phi^{n+1}\}_C]]\end{aligned}$$

Even assuming the linearity hypothesis, in order for the continuity constraint $D[F^{-1}[\{u^{n+1}, v^{n+1}, w^{n+1}\}_C]] = 0$ to be ensured, it should result both $F[N[\cdot]] = I$ and $F[G[\cdot]] = G_c[\cdot]$. Therefore, if one assumes $F = N^{-1}$ from the first condition, it must be verified $N^{-1}[G[\cdot]] = G_c[\cdot]$ from the second one. It is presumable that is not possible to simultaneously fulfil both conditions[‖] and some approximations are consequently introduced. Thus, it is important to assess *a posteriori* the measure of the resulting error, as it is now illustrated.

For reaching this goal, one will proceed by assessing if the sets of normal-face velocities obtained (*a posteriori*) from the linear interpolation of (24), let us say $\{\hat{u}^{n+1}\}_f, \{\hat{v}^{n+1}\}_f, \{\hat{w}^{n+1}\}_f = N[\{u^{n+1}, v^{n+1}, w^{n+1}\}_C]$, allow us to satisfy Equations (17) and (22). This way, one can quantify the error in computing $D[\{\hat{u}^{n+1}\}_f, \{\hat{v}^{n+1}\}_f, \{\hat{w}^{n+1}\}_f]$. Observe that even if such velocities are located onto the same staggered positions of (23), therefore in a MAC-like arrangement, the staggered sets are different.

According to the previous guidelines, one proceeds by taking into account the expressions (23) while substituting in them the intermediate velocities deduced from Equations (24), that is by exploiting the cell-centred discrete HHD $\{u^*, v^*, w^*\}_C = \{u^{n+1}, v^{n+1}, w^{n+1}\}_C + G_c[\{\phi^{n+1}\}_C]$. Thus, after some manipulations, one rewrites the staggered sets (23) as

$$\begin{aligned}
u^{n+1}_{i\pm 1/2,j,k} &\cong \frac{u^{n+1}_{i\pm 1,j,k} + u^{n+1}_{i,j,k}}{2} \pm \Delta t \left(\frac{\phi^{n+1}_{i\pm 2,j,k} + 3\phi^{n+1}_{i,j,k} - 3\phi^{n+1}_{i\pm 1,j,k} - \phi^{n+1}_{i\mp 1,j,k}}{4\Delta x} \right)\\
v^{n+1}_{i,j+1/2,k} &\cong N^{\text{nord}}_{j+1} v^{n+1}_{i,j+1,k} + N^{\text{nord}}_{j} v^{n+1}_{i,j,k} + \Delta t \left[\frac{\phi^{n+1}_{i,j+2,k} N^{\text{nord}}_{j+1}}{y_{j+2} - y_j} - \frac{\phi^{n+1}_{i,j-1,k} N^{\text{nord}}_{j}}{y_{j+1} - y_{j-1}} \right.\\
&\quad \left. + \phi^{n+1}_{i,j+1,k} \left(\frac{N^{\text{nord}}_{j}}{y_{j+1} - y_{j-1}} - \frac{1}{y_{j+1} - y_j} \right) + \phi^{n+1}_{i,j,k} \left(\frac{1}{y_{j+1} - y_j} - \frac{N^{\text{nord}}_{j+1}}{y_{j+2} - y_j} \right) \right]\\
v^{n+1}_{i,j-1/2,k} &\cong N^{\text{sud}}_{j-1} v^{n+1}_{i,j-1,k} + N^{\text{sud}}_{j} v^{n+1}_{i,j,k} + \Delta t \left[\frac{\phi^{n+1}_{i,j+1,k} N^{\text{sud}}_{j}}{y_{j+1} - y_{j-1}} - \frac{\phi^{n+1}_{i,j-2,k} N^{\text{sud}}_{j-1}}{y_j - y_{j-2}} \right.\\
&\quad \left. + \phi^{n+1}_{i,j,k} \left(\frac{N^{\text{sud}}_{j-1}}{y_j - y_{j-2}} - \frac{1}{y_j - y_{j-1}} \right) + \phi^{n+1}_{i,j-1,k} \left(\frac{1}{y_j - y_{j-1}} - \frac{N^{\text{sud}}_{j}}{y_{j+1} - y_{j-1}} \right) \right]\\
w^{n+1}_{i,j,k\pm 1/2} &\cong \frac{w^{n+1}_{i,j,k\pm 1} + w^{n+1}_{i,j,k}}{2} \pm \Delta t \left(\frac{\phi^{n+1}_{i,j,k\pm 2} + 3\phi^{n+1}_{i,j,k} - 3\phi^{n+1}_{i,j,k\pm 1} - \phi^{n+1}_{i,j,k\mp 1}}{4\Delta z} \right)
\end{aligned} \tag{25}$$

[‖] Without going into mathematical details, some properties on the operators are required, for example the symmetry or that they are adjoint.

Thus, one sees that the RHS of expressions (25) are composed of two contributions: the first one is the linear interpolation of the updated cell-centred velocity, i.e. the previously defined sets $\{\hat{u}^{n+1}\}_f, \{\hat{v}^{n+1}\}_f, \{\hat{w}^{n+1}\}_f$, the other one being nothing else but a discretization of the third derivative of the scalar field ϕ^{n+1}, multiplied by the time step and the square of the mesh size, let say $M[\{\phi^{n+1}\}_C]$. Equation (25) can be symbolically indicated as

$$\{u^{n+1}\}_f, \{v^{n+1}\}_f, \{w^{n+1}\}_f = \{\hat{u}^{n+1}\}_f, \{\hat{v}^{n+1}\}_f, \{\hat{w}^{n+1}\}_f + M[\{\phi^{n+1}\}_C]$$

In conclusion, one is now able to rigorously quantify the resulting mass conservation error introduced by the APM formulation. Indeed, it is easy to show that $D[\{\hat{u}^{n+1}\}_f, \{\hat{v}^{n+1}\}_f, \{\hat{w}^{n+1}\}_f] = -D[M[\{\phi^{n+1}\}_C]]$, meaning that the discrete continuity constraint obtained by interpolating (24), i.e. $D[N[\{u^{n+1}, v^{n+1}, w^{n+1}\}_C]]$, is not satisfied up to machine accuracy but provides

$$\begin{aligned} D[N[\{u^{n+1}, v^{n+1}, w^{n+1}\}_C]] = {} & \frac{u^{n+1}_{i+1,j,k} - u^{n+1}_{i-1,j,k}}{2\Delta x} \\ & + \frac{N^{\text{nord}}_{j+1} v^{n+1}_{i,j+1,k} + (N^{\text{nord}}_{j} - N^{\text{sud}}_{j}) v^{n+1}_{i,j,k} - N^{\text{sud}}_{j-1} v^{n+1}_{i,j-1,k}}{h_y} \\ & + \frac{w^{n+1}_{i,j,k+1} - w^{n+1}_{i,j,k-1}}{2\Delta z} = \varepsilon \end{aligned} \tag{26}$$

It is possible to show that the error ε is expressed (for a uniform vertical grid) according to [6, 7]

$$\varepsilon = -\Delta t \left(\frac{\Delta x^2}{4} \frac{\partial^4 \phi}{\partial x^4} + \frac{\Delta y^2}{4} \frac{\partial^4 \phi}{\partial y^4} + \frac{\Delta z^2}{4} \frac{\partial^4 \phi}{\partial z^4} \right) \Bigg|_{i,j,k} + \cdots \tag{27}$$

By concluding the analysis of this part, one can address the following issues existing in the APM:

(1) The velocities $\{u^{n+1}\}_f, \{v^{n+1}\}_f, \{w^{n+1}\}_f$, computed by means of (23), allow us to automatically satisfy the discrete continuity equation (22). They constitute a set of staggered velocities in a MAC-like arrangement but they do not suffice, by alone, to indicate the way to compute the divergence-free cell-centred updated velocities.

(2) The velocities $\{\hat{u}^{n+1}\}_f, \{\hat{v}^{n+1}\}_f, \{\hat{w}^{n+1}\}_f$, computed by means of the linear interpolation of (24), even if located in the same staggered positions of the above sets, produce a local truncation error in the continuity constraint that is first-order in time and second-order in space, see (27). Though the compact stencil (17) has been adopted for eliminating spurious modes in the discrete Laplacian operator, as a result, for fixed mesh size, the continuity error cannot be reduced to zero at machine accuracy.

(3) As a consequence of points (1) and (2), if the convective fluxes in Equation (7) were computed while exploiting the non-solenoidal sets $\{\hat{u}^{n+1}\}_f, \{\hat{v}^{n+1}\}_f, \{\hat{w}^{n+1}\}_f$ (coming

> from linear interpolation of cell-centred values) instead of using directly the divergence-free velocities (23), that is the sets $\{u^{n+1}\}_f, \{v^{n+1}\}_f, \{w^{n+1}\}_f$, the continuity error can propagate during the other time steps by the way of the computation of momentum equation. It is well known that the error in the continuity acts as a source term in the (derived) balance of kinetic energy equation and destroy the conservation property (in the inviscid limit) as well as this action can drive to the numerical instability of the calculation.

Let us introduce the new ideas of the formulation, the aim being now clear: to eliminate the errors addressed in points (2) and (3). Therefore, one can think of a suitable modification of the approximate projection method.

5.2. The EPM framework: exact two-steps (DPM) correction

As a consequence of the above issues (2), (3), it is advisable to improve the APM procedure in order for obtaining the discrete continuity constraint better ensured. The new idea, proposed in this paper, consists of introducing a correction that, instead of exploiting the dissipative MIM procedure [6, 15, 16], directly exploits the guidelines of the HHD theorem [18]. Actually, the MIM procedure uses both an *ad hoc* term that smoothes the oscillations produced by the fourth-order derivatives in (27) and the dissipative QUICK discretization that adds a further smoothing of vorticity. Thus, the main idea is to deduce a specific correction that, while ensuring the mass conservation up to machine accuracy, uses a suitable second gradient field, since it would not alter the vorticity field.

The main task will consist in exploiting the HHD decomposition in order to introduce an additional scalar field, defined in the FV centres, i.e. let us say the set $\{f^{n+1}\}_C$, such that its discrete gradient $G_c[\{f^{n+1}\}_C]$ corrects (24) while allowing to make (26) vanishing. Such a correction is defined only in a discrete sense and is derived only after the APM discretization is introduced. Since the goal is to ensure the continuity constraint satisfied up to machine precision, one can see this procedure in the framework of the EPM formulation. A suitable construction of the algorithm is anyway required in order to avoid the well-known plague of the presence of spurious non-solenoidal modes. Therefore, the improved procedure is now generally addressed as DPM formulation to distinguish from the classical EPM one. Furthermore, the HHD theorem allows us to prescribe a second elliptic problem therefore, the present DPM procedure well accords in the framework of the two-steps procedure reported in Reference [9] and is now illustrated directly for the case of a non-uniform 3D structured grid.

Let us assume having already solved the APM step, from which one possesses the set $\{u^*, v^*, w^*, \phi^{n+1}\}_C$. Since the updated velocity components (24) do not result divergence-free, let us indicate such approximation by using the tilde symbol onto the APM-based updated velocity, thus rewriting (24) according to $\tilde{\mathbf{v}}_{i,j,k}^{n+1} = \mathbf{v}_{i,j,k}^{*} - \Delta t \underline{\nabla}\phi|_{i,j,k}^{n+1}$. Therefore, the HHD theorem ensures that $\tilde{\mathbf{v}}_{i,j,k}^{n+1}$ can be further decomposed in a (discretely) exact divergence-free and in a curl-free vector fields according to $\tilde{\mathbf{v}}_{i,j,k}^{n+1} = \mathbf{v}_{i,j,k}^{n+1} + \Delta t \underline{\nabla} f|_{i,j,k}^{n+1}$. It is a simple task combining the expressions and rewriting the HHD as $\mathbf{v}_{i,j,k}^{n+1} = \mathbf{v}_{i,j,k}^{*} - \Delta t(\underline{\nabla}\phi|_{i,j,k}^{n+1} + \underline{\nabla} f|_{i,j,k}^{n+1}) = \mathbf{v}_{i,j,k}^{*} - \Delta t \underline{\nabla}\Psi|_{i,j,k}^{n+1}$

that is discretized according to

$$\begin{aligned}
u^{n+1}_{i,j,k} &= u^{*}_{i,j,k} - \Delta t\left(\frac{\phi^{n+1}_{i+1,j,k}-\phi^{n+1}_{i-1,j,k}}{2\Delta x}\right) - \Delta t\left(\frac{f^{n+1}_{i+1,j,k}-f^{n+1}_{i-1,j,k}}{2\Delta x}\right)\\
v^{n+1}_{i,j,k} &= v^{*}_{i,j,k} - \Delta t\left(\frac{\phi^{n+1}_{i,j+1,k}-\phi^{n+1}_{i,j-1,k}}{y_{j+1}-y_{j-1}}\right) - \Delta t\left(\frac{f^{n+1}_{i,j+1,k}-f^{n+1}_{i,j-1,k}}{y_{j+1}-y_{j-1}}\right)\\
w^{n+1}_{i,j,k} &= w^{*}_{i,j,k} - \Delta t\left(\frac{\phi^{n+1}_{i,j,k+1}-\phi^{n+1}_{i,j,k-1}}{2\Delta z}\right) - \Delta t\left(\frac{f^{n+1}_{i,j,k+1}-f^{n+1}_{i,j,k-1}}{2\Delta z}\right)
\end{aligned} \tag{28}$$

Of course, the first and second addends in the RHS of (28) are known terms while the LHS is the desired effective new velocity field. The new scalar field f^{n+1} is now prescribed to be solution of an elliptic equation with a source term suitably constructed in such a way to absorb the continuity error in (26). Specifically, if the expressions (28) are symbolically rewritten as

$$\begin{aligned}
\{u^{n+1}, v^{n+1}, w^{n+1}\}_C &= \{\tilde{u}^{n+1}, \tilde{v}^{n+1}, \tilde{w}^{n+1}\}_C - G_c[\{\phi^{n+1}\}_C]\\
&= \{u^{*}, v^{*}, w^{*}\}_C - G_c[\{\phi^{n+1}\}_C] - G_c[\{f^{n+1}\}_C]
\end{aligned}$$

then, projecting the sets of interpolated normal-to-face velocities $N[\{u^{n+1}, v^{n+1}, w^{n+1}\}_C]$ into the sub-space of divergence-free functions, that is setting $D[N[\{u^{n+1}, v^{n+1}, w^{n+1}\}_C]] = \varepsilon = 0$, one gets the second elliptic equation

$$D[N[G_c[\{f^{n+1}\}_C]]] = D[N[\{u^{*}, v^{*}, w^{*}\}_C] - N[G_c[\{\phi^{n+1}\}_C]]]$$

the solution set $\{f^{n+1}\}_C$ being finally able to satisfy continuity (26). The discrete elliptic equation for the scalar field f explicitly writes as

$$\begin{aligned}
&-\frac{f^{n+1}_{i,j,k}}{2}\left[\frac{1}{\Delta x^2}+\frac{1}{\Delta z^2}+\frac{1}{\Delta y_{j+1}(y_{j+2}-y_j)}+\frac{1}{\Delta y_j(y_j-y_{j-2})}\right]\\
&\quad+\frac{f^{n+1}_{i+2,j,k}+f^{n+1}_{i-2,j,k}}{4\Delta x^2}+\frac{f^{n+1}_{i,j,k+2}+f^{n+1}_{i,j,k-2}}{4\Delta z^2}+\frac{f^{n+1}_{i,j+1,k}-f^{n+1}_{i,j-1,k}}{2(y_{j+1}-y_{j-1})}\\
&\quad\times\left(\frac{1}{\Delta y_j}-\frac{1}{\Delta y_{j+1}}\right)+\frac{f^{n+1}_{i,j+2,k}}{2\Delta y_{j+1}(y_{j+2}-y_j)}+\frac{f^{n+1}_{i,j-2,k}}{2\Delta y_j(y_j-y_{j-2})}\\
&\quad=-\left[\frac{\phi^{n+1}_{i+2,j,k}-2\phi^{n+1}_{i,j,k}+\phi^{n+1}_{i-2,j,k}}{4\Delta x^2}+\frac{N^{\text{nord}}_{j+1}}{h_y}\left(\frac{\phi^{n+1}_{i,j+2,k}-\phi^{n+1}_{i,j,k}}{y_{j+2}-y_j}\right)\right.
\end{aligned}$$

$$
\begin{aligned}
&+\frac{(N_j^{\mathrm{nord}}-N_j^{\mathrm{sud}})}{h_y}\left(\frac{\phi^{n+1}_{i,j+1,k}-\phi^{n+1}_{i,j-1,k}}{y_{j+1}-y_{j-1}}\right)-\frac{N^{\mathrm{sud}}_{j-1}}{h_y}\left(\frac{\phi^{n+1}_{i,j,k}-\phi^{n+1}_{i,j-2,k}}{y_j-y_{j-2}}\right)\\
&+\frac{\phi^{n+1}_{i,j,k+2}-2\phi^{n+1}_{i,j,k}+\phi^{n+1}_{i,j,k-2}}{4\Delta z^2}\Bigg]+\frac{1}{\Delta t}\Bigg[\frac{u^*_{i+1,j,k}-u^*_{i-1,j,k}}{2\Delta x}\\
&+\frac{N^{\mathrm{nord}}_{j+1}v^*_{i,j+1,k}+(N^{\mathrm{nord}}_j-N^{\mathrm{sud}}_j)v^*_{i,j,k}-N^{\mathrm{sud}}_{j-1}v^*_{i,j-1,k}}{h_y}+\frac{w^*_{i,j,k+1}-w^*_{i,j,k-1}}{2\Delta z}\Bigg]
\end{aligned}
\tag{29}
$$

Equation (29) must be associated to suitable boundary conditions prescribed in order to satisfy the compatibility condition, ensuring the existence of a solution f^{n+1} (apart a constant). Therefore, since according to Equation (18) one has

$$
\left.\frac{\partial f}{\partial y}\right|^{n+1}_{i,j_{\mathrm{bnd}},k}=-\left.\frac{\partial \phi}{\partial y}\right|^{n+1}_{i,j_{\mathrm{bnd}},k}+\frac{1}{\Delta t}(v^*_{i,j_{\mathrm{bnd}},k}-v^{n+1}_{i,j_{\mathrm{bnd}},k})=0
\tag{30}
$$

homogeneous Neumann boundary conditions must be prescribed at $j_{\mathrm{bnd}}=1$ and $j_{\mathrm{bnd}}=m$. The correct implementation of these boundary conditions involves a careful rewriting of Equation (29). As an example, let us consider the equation that must be written at a point (not involving periodic boundary conditions that are implemented as illustrated in the previous section) having $\bar{j}=m-1$ (see Figure 2). Hence, rewrite the procedure starting from Equation (26), setting $\varepsilon=0$ while imposing the correct normal velocity component on the boundary, that is $v^{n+1}_{i,m,k}$, substituting (28) and exploiting (30)

$$
\begin{aligned}
&\frac{u^{n+1}_{i+1,m-1,k}-u^{n+1}_{i-1,m-1,k}}{2\Delta x}+\frac{v^{n+1}_{i,m,k}-(N^{\mathrm{sud}}_{m-1}v^{n+1}_{i,m-1,k}+N^{\mathrm{sud}}_{m-2}v^{n+1}_{i,m-2,k})}{h_y}\\
&\quad+\frac{w^{n+1}_{i,m-1,k+1}-w^{n+1}_{i,m-1,k-1}}{2\Delta z}=0\\
&=\frac{u^*_{i+1,m-1,k}-u^*_{i-1,m-1,k}}{2\Delta x}+\frac{v^{n+1}_{i,m,k}-(N^{\mathrm{sud}}_{m-1}v^*_{i,m-1,k}+N^{\mathrm{sud}}_{m-2}v^*_{i,m-2,k})}{h_y}\\
&\quad+\frac{w^*_{i,m-1,k+1}-w^*_{i,m-1,k-1}}{2\Delta z}-\Delta t\Bigg[\frac{\phi^{n+1}_{i+2,m-1,k}-2\phi^{n+1}_{i,m-1,k}+\phi^{n+1}_{i-2,m-1,k}}{4\Delta x^2}\\
&\quad-\frac{N^{\mathrm{sud}}_{m-1}}{h_y}\left(\frac{\phi^{n+1}_{i,m,k}-\phi^{n+1}_{i,m-2,k}}{y_m-y_{m-2}}\right)-\frac{N^{\mathrm{sud}}_{m-2}}{h_y}\left(\frac{\phi^{n+1}_{i,m-1,k}-\phi^{n+1}_{i,m-3,k}}{y_{m-1}-y_{m-3}}\right)\\
&\quad+\frac{\phi^{n+1}_{i,m-1,k+2}-2\phi^{n+1}_{i,m-1,k}+\phi^{n+1}_{i,m-1,k-2}}{4\Delta z^2}+\frac{f^{n+1}_{i+2,m-1,k}-2f^{n+1}_{i,m-1,k}+f^{n+1}_{i-2,m-1,k}}{4\Delta x^2}
\end{aligned}
$$

$$
\begin{aligned}
&-\frac{N^{\mathrm{sud}}_{m-1}}{h_y}\left(\frac{f^{n+1}_{i,m,k}-f^{n+1}_{i,m-2,k}}{y_m-y_{m-2}}\right)-\frac{N^{\mathrm{sud}}_{m-2}}{h_y}\left(\frac{f^{n+1}_{i,m-1,k}-f^{n+1}_{i,m-3,k}}{y_{m-1}-y_{m-3}}\right)\\
&\left.+\frac{f^{n+1}_{i,m-1,k+2}-2f^{n+1}_{i,m-1,k}+f^{n+1}_{i,m-1,k-2}}{4\Delta z^2}\right] \qquad (31)
\end{aligned}
$$

so that, one gets the equation that takes into account the inclusion of the boundary condition (30)

$$
\begin{aligned}
&-\frac{f^{n+1}_{i,m-1,k}}{2}\left[\frac{1}{\Delta x^2}+\frac{1}{\Delta z^2}+\frac{1}{\Delta y_{m-1}(y_{m-1}-y_{m-3})}\right]+\frac{f^{n+1}_{i+2,m-1,k}+f^{n+1}_{i-2,m-1,k}}{4\Delta x^2}\\
&+\frac{f^{n+1}_{i,m-1,k+2}+f^{n+1}_{i,m-1,k-2}}{4\Delta z^2}-\left(\frac{1}{h_y}-\frac{1}{2\Delta y_{m-1}}\right)\left(\frac{f^{n+1}_{i,m,k}-f^{n+1}_{i,m-2,k}}{y_m-y_{m-2}}\right)\\
&+\frac{f^{n+1}_{i,m-3,k}}{2\Delta y_{m-1}\,(y_{m-1}-y_{m-3})}=-\left[\frac{\phi^{n+1}_{i+2,m-1,k}-2\phi^{n+1}_{i,m-1,k}+\phi^{n+1}_{i-2,m-1,k}}{4\Delta x^2}\right.\\
&-\frac{N^{\mathrm{sud}}_{m-1}}{h_y}\left(\frac{\phi^{n+1}_{i,m,k}-\phi^{n+1}_{i,m-2,k}}{y_m-y_{m-2}}\right)-\frac{N^{\mathrm{sud}}_{m-2}}{h_y}\left(\frac{\phi^{n+1}_{i,m-1,k}-\phi^{n+1}_{i,m-3,k}}{y_{m-1}-y_{m-3}}\right)\\
&\left.+\frac{\phi^{n+1}_{i,m-1,k+2}-2\phi^{n+1}_{i,m-1,k}+\phi^{n+1}_{i,m-1,k-2}}{4\Delta z^2}\right]+\frac{1}{\Delta t}\left[\frac{u^{*}_{i+1,m-1,k}-u^{*}_{i-1,m-1,k}}{2\Delta x}\right.\\
&\left.+\frac{v^{n+1}_{i,m,k}-\left(N^{\mathrm{sud}}_{m-1}v^{*}_{i,m-1,k}+N^{\mathrm{sud}}_{m-2}v^{*}_{i,m-2,k}\right)}{h_y}+\frac{w^{*}_{i,m-1,k+1}-w^{*}_{i,m-1,k-1}}{2\Delta z}\right] \qquad (32)
\end{aligned}
$$

However, owing to the large stencil, it is still necessary to prescribe in (32) a suitable condition for expressing the value $f^{n+1}_{i,m,k}$ while respecting (30). It is worthwhile reminding that in determining Equation (21), the boundary condition for the scalar field ϕ^{n+1} never required a discretization of Equation (18) but this latter has been directly used in its continuous form. This fact allows us some degree of freedom for setting the last condition. In fact, though a higher order relation can be used, a congruent discretization that verifies the compatibility condition could be simply imposed by setting $f^{n+1}_{i,m,k}=f^{n+1}_{i,m-1,k}$. Accordingly Equation (30) is discretized as

$$
\left(\frac{f^{n+1}_{i,m,k}-f^{n+1}_{i,m-1,k}}{y_m-y_{m-1}}\right)=-\left(\frac{\phi^{n+1}_{i,m,k}-\phi^{n+1}_{i,m-1,k}}{y_m-y_{m-1}}\right)+\frac{1}{\Delta t}(v^{*}_{i,m,k}-v^{n+1}_{i,m,k})=0 \qquad (33)
$$

therefore one must set $\phi^{n+1}_{i,m,k}=\phi^{n+1}_{i,m-1,k}+(y_m-y_{m-1})(v^{*}_{i,m,k}-v^{n+1}_{i,m,k})/\Delta t$ in the RHS of (32). As a consequence, the multiplier of $-f^{n+1}_{i,m-1,k}/2$ in Equation (32) has to be modified by adding $+[1/h_y-1/(2\Delta y_{m-1})][2/(y_m-y_{m-2})]$ to the terms in square brackets while, of course, the out-main diagonal contribute of $f^{n+1}_{i,m,k}$ vanishes. Furthermore, since in Equation (29) appears the unknown $f_{i,j+2,k}$, the equations at points having $j=m-2$ must be also congruently modified by setting again $f^{n+1}_{i,m,k}=f^{n+1}_{i,m-1,k}$ and changing the correspondent coefficient. Analogously, one proceeds for the bottom points at $j=2$ and $j=3$ and this specific treatment of the discrete boundary conditions fulfils the compatibility condition and the existence of a solution f is ensured. It is now clear that one is sure that $D[N[\{u^{n+1},v^{n+1},w^{n+1}\}_C]]=0$ everywhere.

The DPM procedure is now completed since, after solving the second elliptic equation and computing the (28), one possesses both the previous MAC-like staggered divergence-free sets $\{u^{n+1}\}_f, \{v^{n+1}\}_f, \{w^{n+1}\}_f$ and the new set of collocated and divergence-free $\{u^{n+1},v^{n+1},w^{n+1}\}_C$ velocities (one can disregard the APM-based one $\{\tilde{u}^{n+1},\tilde{v}^{n+1},\tilde{w}^{n+1}\}_C$) that allow us completing the cycle and going to the next time step.

It is worthwhile observing that this procedure is not limited to structured Cartesian grids but can be extended to unstructured triangular (tetrahedral in 3D) grids. For example, considering for the sake of brevity a decomposition of a 2D domain in K^{T} triangles, a dual tassellation in N Finite Volumes Ω_i of the domain Ω is defined so that $\{\Omega_i\}:\Omega=\bigcup_{i=1}^{N}\Omega_i, \Omega_i\bigcap\Omega_j=\{0\}\forall i\neq j$ over which the NS equations (1), (2) are solved according to the APM formulation proposed in Reference [21]. Thus, the counterpart of Equations (24) becomes

$$\tilde{\mathbf{v}}_i^{n+1}=\mathbf{v}_i^{*}-\frac{\Delta t}{|\Omega_i|}\sum_{l=1}^{b_i}\int_{P_l}^{Q_l}\mathbf{n}_l\phi^{n+1}\,\mathrm{d}S_l \tag{34}$$

where b_i is the number of edges $\partial\Omega_{il}=P_l-Q_l$ composing the ith FV boundary $\partial\Omega_i=\bigcup_{l=1}^{b_i}\partial\Omega_{il}$ and $\mathbf{n}_l$ is the outward-oriented unit normal vector to the lth section $\partial\Omega_{il}$. Since one gets the approximate continuity constraint $\sum_{l=1}^{b_i}\int_{P_l}^{Q_l}\mathbf{n}_l\cdot\tilde{\mathbf{v}}^{n+1}\,\mathrm{d}S_l=O(\mathrm{LTE})$, the second elliptic equation must, therefore, provide a correction expressed by a gradient field such that the discrete constraint is ensured in terms of the updated velocity field $\mathbf{v}_i^{n+1}$, that is

$$\int_{\partial\Omega_i}\mathbf{n}\cdot\mathbf{v}^{n+1}\,\mathrm{d}S=\sum_{l=1}^{b_i}\int_{P_l}^{Q_l}\mathbf{n}_l\cdot\tilde{\mathbf{v}}^{n+1}\,\mathrm{d}S_l-O(\mathrm{LTE})=0 \tag{35}$$

while according to the HHD $\mathbf{v}_i^{n+1}=\tilde{\mathbf{v}}_i^{n+1}-(\Delta t/|\Omega_i|)\int_{\partial\Omega_i}\mathbf{n}f^{n+1}\,\mathrm{d}S$. Of course, a suitable discretization of the line integrals in order for (35) to be ensured is necessary. Specifically, it is necessary to build a second tassellation being, however, $\Omega_i'\bigcap\Omega_j'\neq\{0\}\forall i\neq j$ since a large computational stencil is required. This extension of the DPM results rather long to be addressed in few words and it is out of the aim of the present paper to illustrate all details.

6. GENERAL DISCUSSION ON THE DPM APPROACH: STABILITY AND ACCURACY

The previously illustrated DPM formulation has the goal of ensuring the continuity constraint fulfilled up to machine accuracy while reducing the possibility of generating spurious high-frequency non-divergent modes. Perhaps, spurious oscillations can be significant in both the EPM and APM procedures and must be controlled in order for physically relevant solutions to be obtained. It is just the way of controlling the non-solenoidal modes that discerns the benefits of a specific correction over other ones. In this sense, the goal of the DPM is similar to that designed by means of the projection filters-based approach for the APM [14].

However, projection-filters were designed in order to diffuse non-solenoidal modes by means of diffusive-like operators (the main diagonal part of a Jacobi-like relaxation is used) but they are not designed to exactly ensure the continuity. The two-steps elliptic formulation proposed in Reference [8] is similarly designed since the discrete approximation of fourth-order accurate elliptic operator acts in order for high-frequency modes to be dissipated but the continuity constraint still remains approximated. Thus, one can still speak of these two formulations as APM-based and although are very popular for solving the incompressible form of the NS equations, they are not without own problems.

The importance of both ensuring the satisfaction of the mass equation and avoiding spurious modes, while not adding numerical dissipation, is particularly relevant in the DNS/LES formulations whereas the computations are performed for long time and the solution remains unsteady. In general, even when the computational parameters satisfy the linear stability constraints, producing a mass error can be extremely damaging for the stability of the simulations. In fact, the kinetic energy is not a resolved quantity but it is induced by the discrete momentum quantity (e.g. see Reference [6]). Thus, producing a local mass error (even if the surface integral mass were conserved) has its counterpart in introducing a source term in the kinetic energy equation in the form of work done by the pressure, i.e. $p\underline{\nabla}\cdot\mathbf{v}$. This effect is very dangerous for long-term integration since, the lack of the kinetic energy conservation (in the non-viscous limit) can increase the total amount of energy. This increasing can be also responsible for a numerical instability not analysable by the linear numerical stability theory for a single scalar equation. Therefore, one must contrast instability due both to high frequency errors (e.g. round-off) propagating in the non-linear momentum equation and to the increasing of total energy, not necessarily corresponding to high frequencies.

Along with the continuity errors an important issue to be analysed is the stability of the projection method for which it is required that the projector be bounded in some norm [9, 13, 14, 22]. Hence, while defining the EPM-based projector P_H such that $\mathbf{v}^{n+1}=P_H(\mathbf{v}^*)$, $\underline{\nabla}\cdot\mathbf{v}^{n+1}=0$, it is well known that it is symmetric, idempotent and bounded, that is $S(P_H)\triangleq\sup_{\mathbf{x}\neq\mathbf{0}}(\|P_H(\mathbf{x})\|/\|\mathbf{x}\|)\leqslant 1$. On the other hand, the (approximate) projection operator acting in the APM, say P, is such that $\tilde{\mathbf{v}}^{n+1}=P(\mathbf{v}^*)$, $\underline{\nabla}\cdot\tilde{\mathbf{v}}^{n+1}\neq 0$ but P is no longer idempotent although $(P)^k\to P_H$ as $k\to\infty$. There is a wide literature on the stability properties of approximate projection methods and the results are sometimes not always concordant. It is out of the aims of the present paper to develop the stability theory, here it is worthwhile addressing that it can be shown that the DPM projector is the product of the APM and EPM ones, that is $\mathbf{v}^{n+1}=P_{\mathrm{DPM}}(\mathbf{v}^*)\triangleq P_H[P(\mathbf{v}^*)]$, and P_{DPM} is symmetric, idempotent as well as bounded. Hence, concerning the DPM formulation one can consider valid the well known stability properties of the projection methods already analysed in several studies. On the other hand, in case of periodic conditions, one can consequently state that the DPM would reduce to nothing else but a single EPM on a large stencil. In other words, one could be tempted to directly redefine (11) while solving directly the elliptic equation for computing the field $\underline{\nabla}\Psi|_{i,j,k}^{n+1}$, without first performing the APM step. However, such an elliptic equation would be defined on a checkerboard stencil that produces spurious solutions. The fact that, instead of using only $\underline{\nabla}\Psi|_{i,j,k}^{n+1}$, one use both fields $(\underline{\nabla}\phi|_{i,j,k}^{n+1},\underline{\nabla}f|_{i,j,k}^{n+1})$ allows us to couple the compact with the large stencil by means of the MAC-like staggered velocities $\{u^{n+1}\}_f,\{v^{n+1}\}_f,\{w^{n+1}\}_f$ provided by the APM step. Furthermore, one can see that for confined flows, such as those characterized by the buoyancy in which we are interested in, the stencil of the second elliptic solver is suitably constructed near the boundary and all nodes along the y direction are coupled. This can be seen by observing that in (32) the next values $f^{n+1}_{i,m-1,k}, f^{n+1}_{i,m-2,k}, f^{n+1}_{i,m-3,k}$ are simultaneously present, corresponding to the elimination in the y direction of a spurious zero in Fourier symbol.

After the stability of the projection method, let us now consider the stability analysis of the discrete intermediate momentum equation. In order to examine the characteristics of weak numerical instability present in the explicit AB integration along with the stabilizing features** of the implicit CN scheme (adopted along the y-direction) a linear stability analysis is now performed. Let us consider (for the sake of brevity for the 2D case) the second-order accurate central space discretization for the convection–diffusion linear balance equation $(\partial\varphi/\partial t) + \mathbf{v}\cdot\underline{\nabla}\varphi = \Gamma\nabla^2\varphi$, ($u$, v, Γ are assumed constant)

$$\begin{aligned}
&\left[I - \frac{\beta_y}{2}(E^{\Delta y} - 2I + E^{-\Delta y})\right]\varphi^{n+1}_{i,j}\\
&\quad = \left[I + \frac{\beta_y}{2}(E^{\Delta y} - 2I + E^{-\Delta y})\right]\varphi^{n}_{i,j}\\
&\quad -\frac{3}{2}\left[c_x\frac{E^{\Delta x} - E^{-\Delta x}}{2} + c_y\frac{E^{\Delta y} - E^{-\Delta y}}{2} - \beta_x(E^{\Delta x} - 2I + E^{-\Delta x})\right]\varphi^{n}_{i,j}\\
&\quad +\frac{1}{2}\left[c_x\frac{E^{\Delta x} - E^{-\Delta x}}{2} + c_y\frac{E^{\Delta y} - E^{-\Delta y}}{2} - \beta_x(E^{\Delta x} - 2I + E^{-\Delta x})\right]\varphi^{n-1}_{i,j}
\end{aligned}\tag{36}$$

where the shift notation has been introduced and $\beta_x = \Gamma\Delta t/\Delta x^2$, $\beta_y = \Gamma\Delta t/\Delta y^2$, $c_x = u\Delta t/\Delta x$, $c_y = v\Delta t/\Delta y$. Equation (36) can be written in the matrix notation as $\mathbf{A}\cdot\mathbf{z}^{n+1} = \mathbf{B}\cdot\mathbf{z}^n$ being the auxiliary vector $\mathbf{z} = [\varphi, z]^{\mathrm{T}}$ and $z^n = \varphi^{n-1}$. The Von Neumann stability analysis is carried out by substituting the Fourier component $\hat{E}(t)\mathrm{e}^{\mathbf{ik}\cdot\mathbf{x}}$, $\mathbf{k}$ being the wavenumber vector, into the corresponding error evolution equation and by determining the two eigenvalues of the amplification matrix $\mathbf{G} = \mathbf{A}^{-1}\cdot\mathbf{B}$. The eigenvalues are the zeros of the Von Neumann polynomial and they must be lower than one in modulus for the stability condition. It is well known that the AB integration alone leads to a weak instability because one of the two eigenvalues is slightly greater than one in modulus. The effect of the implicit part, in terms of global stability, has been analysed for several combinations of the integration parameters and the locus wherein the second eigenvalue has a unitary modulus, that is $|\lambda_2|(c_x, c_y, Re_{\Delta x}, Re_{\Delta y}) = 1$, has been computed. Because of the complication in representing the resulting hyper-surface, only its intersections with the planes $c_x = 0$, $c_y = 0$ and $c_x = c_y$, respectively, are presented. These curves, are shown in Figure 3 versus the cell Reynolds number $Re_{\Delta x} = u\Delta x/v$. The linear analysis predicts that the stability region enlarges for high $Re_{\Delta x}$ values. However, it is also well known that second-order central discretization suffer for the presence of oscillations (Godunov theorem precludes the existence of a monotonic solution for linear second order discretization) for increasing $Re_{\Delta x}$ values therefore, it is recommended to adopt a moderate cell Reynolds number for NS computations.

** As a matter of fact, Crank–Nicolson discretization can generate oscillations in the numerical solution owing to oscillatory decay.

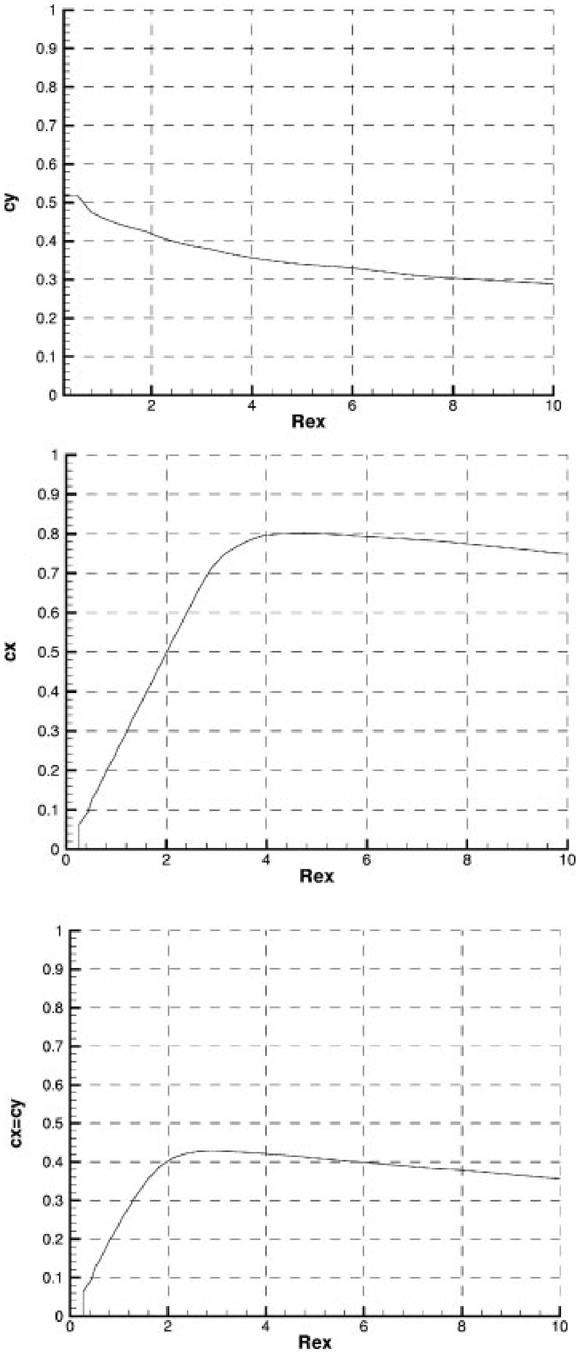

Figure 3. Stability regions for the second-order space-centred, AB/CN time discretization of a 2D convection–diffusion linear equation. Courant number vs the cell Reynolds number: intersections with the planes $c_x = 0$, $c_y = 0$ and $c_x = c_y$.

Finally, before presenting the results for a buoyancy-driven flow, a numerical accuracy study is now performed while exploiting the Taylor vortex-decaying analytical solution, see References [10, 12, 18]. The aim of this test is to analyse the real accuracy of the formulations as well as the stability behaviour and the regularity in terms of the y-edge non-divergent line modes. The test case is performed in the non-dimensional domain $V=[0,2\pi]\times[0,1]$ at unitary Reynolds number. The choice of this domain is motivated by the fact that the analytical solution produces a decomposition (11) that is not orthogonal over it therefore the error in the pressure field can enter into the velocity one, by making the test more critical than it would be in a domain where the decomposition is orthogonal, see Reference [12]. Periodic boundary conditions are prescribed only in x-direction while Dirichlet ones are imposed at $y=0$, $y=1$. An optimized SOR procedure is used in all tests for solving the elliptic equations and a tolerance of 10^{-9} for both iterative solvers, to be reached by the L_2 norm of the residual, is fixed. Actually, while using an iterative method the continuity constraint is not satisfied up to machine accuracy but only up to the magnitude order of the residual. Of course, this must not be considered a flaw of the DPM formulation but is just an approximation that can be avoided by using a direct method instead of an iterative one. The integration is continued up to the time $T=0.3$ and the convergence test is performed by reducing progressively the mesh size h, maintained uniform in both directions, from the value $h=1/10$ up to $1/50$ while taking constant the rate $\Delta t/h=2.5\times10^{-3}$, that is a sufficiently small value to ensure the numerical stability. The L_∞ norm is used in the evaluation of the discretization errors since it is sensible to measure local oscillations. The convergence curve obtained for the vertical velocity is reported in Figure 4 for EPM, APM and DPM formulations in a double logarithmic scale. The results clearly illustrate that EPM is far from the expected second-order convergence owing to the fact that the L_∞ norm signals errors near the boundaries and oscillations appear everywhere. Some improvements could be obtained by using a different stencil near the boundary but oscillations still are present. Conversely, the APM formulation produces second-order convergence as well as is reached by DPM that, however, appears slightly better in terms of magnitude.

It is worthwhile reporting some results about the computational efficiency of the DPM procedure. The second elliptic equation is solved by means of the same iterative (SOR) solver used for the first one, while stopping at the same tolerance level. Owing to the second-order discretization, there is almost the same number of operations as the first solver, the difference being in the bands of the matrix caused by the different stencil. During the time integration of the Taylor test-case, the number of cycles necessary in the second solver to reach the tolerance (for an optimal relaxation factor) has been systematically one-third of that one required by the first solver. Moreover, it was also observed that a less stringent tolerance could be used without altering the resulting accuracy, for example three orders of magnitude greater has been sufficient to produce a good level of the continuity error.

However, for a unitary Reynolds number, this result cannot be considered exhaustive of all real features of the formulations since the whole wavenumbers range is well resolved also on the coarsest grid (that is the cell-based Reynolds number is always less than one). Furthermore, the Taylor solution depicts an energy-decaying flow and the behaviour of a long-term integration can be less relevant. A specific application of the method in a buoyancy-driven is thus presented since the energy is continuously transformed from thermal into kinetic form.

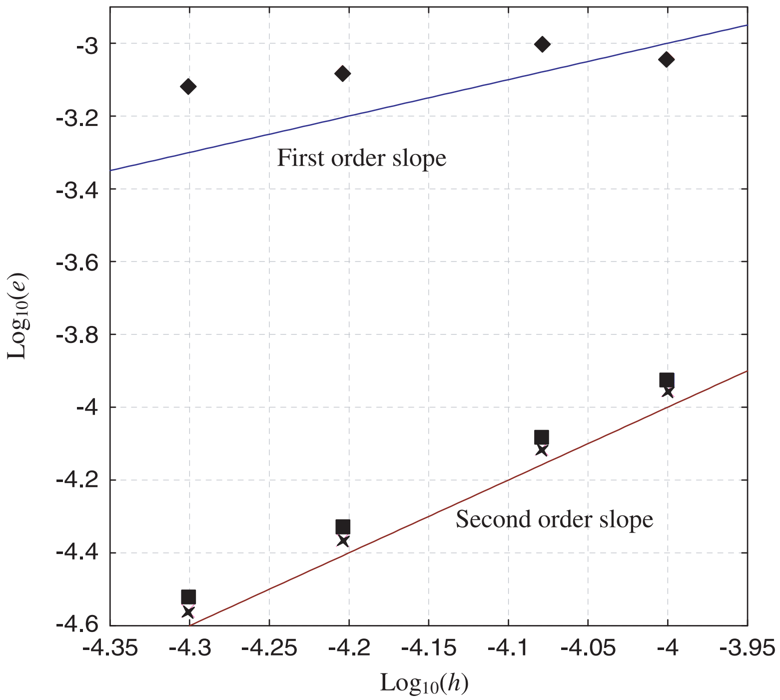

Figure 4. Taylor-vortex problem at unitary Reynolds number. Convergence curves of the vertical velocity errors in the L_∞ norm, reported in a double logarithmic scales, for the EPM (diamond), APM (square), DPM (star).

7. PERFORMANCES OF APM AND DPM FORMULATIONS ON THERMALLY BUOYANCY-DRIVEN FLOW

In this section, the simulations of a thermal convection flow generated by surface cooling in a finite-depth stably stratified horizontal layer, with isothermal bottom surface, are illustrated. This flow is a simple prototype of convection occurring in the ocean during adverse weather events that generates turbulence in response to cold air outbreak, e.g. see Reference [20]. However, owing to the code-validation goal, here we focus only on laminar unsteady conditions. A homogeneous and steady heat flux is prescribed at the upper surface to produce the cooling of an initial stratified flow, corresponding to a constant temperature gradient along the depth and resulting in a hydrostatic equilibrium. Therefore, the convective motions are generated solely by the buoyancy mechanism caused by inhomogeneities in the temperature field. Such flow can be seen in the framework of the Rayleigh–Bénard flows. There is a first phase dominated by linear diffusion of temperature that causes an increasing thickness of the thermal boundary layer until to a time for which the upper cooled layers, once became much denser than the lower one, can no longer be sustained and generate instability so that convective plumes are convected towards the bottom.

The reason that motivated the choice of this kind of flow is twofold. From a side, one has the critical task of reproducing a driving force that acts along the non-uniform direction as a normal stress therefore, it is fundamentally a good resolution of the pressure-like field. Furthermore, the absence of a mean shear flow allows us to better discern the presence of spurious oscillations corresponding to non-solenoidal modes along the y direction. Secondly, this kind of flow does not reach a steady state but the kinetic energy level evolves. The fact that this is not a simple energy-decaying flow (as in the Taylor solution) allows us to experiment the superimposed effects due to the presence of continuity errors that could drive to a numerical instability caused by a non-physical increasing of kinetic energy produced by the work done by pressure.

7.1. Governing equations and flux discretization of convective terms

A Cartesian domain V, having non-dimensional extensions $L_y = 1$, $L_x = L_z = \pi/2$, is used and the governing NS equations are rewritten including the balance of the temperature while employing the Bousinnesq approximation for coupling the buoyancy term, the gravity g acting along the y direction. Hence, the non-dimensional equations write in a FV as

$$\frac{1}{|\Omega(\mathbf{x})|}\int_{\partial\Omega(\mathbf{x})} \mathbf{n}\cdot\mathbf{v}\,\mathrm{d}S = 0 \tag{37}$$

$$\begin{aligned}\frac{\partial \mathbf{v}}{\partial t} + \frac{1}{|\Omega(\mathbf{x})|}\int_{\partial\Omega(\mathbf{x})} \mathbf{n}\cdot(\mathbf{v}\mathbf{v})\,\mathrm{d}S + \frac{1}{|\Omega(\mathbf{x})|}\int_{\partial\Omega(\mathbf{x})} \mathbf{n}p\,\mathrm{d}S \\ = \frac{2}{Re|\Omega(\mathbf{x})|}\int_{\partial\Omega(\mathbf{x})} \mathbf{n}\cdot\underline{\nabla}^s\mathbf{v}\,\mathrm{d}S - \mathbf{j}Ra(\vartheta_h - \vartheta)\end{aligned} \tag{38}$$

$$\frac{\partial \vartheta}{\partial t} + \frac{1}{|\Omega(\mathbf{x})|}\int_{\partial\Omega(\mathbf{x})} \mathbf{n}\cdot(\mathbf{v}\vartheta)\,\mathrm{d}S = \frac{1}{RePr|\Omega(\mathbf{x})|}\int_{\partial\Omega(\mathbf{x})} \mathbf{n}\cdot\underline{\nabla}\vartheta\,\mathrm{d}S \tag{39}$$

having adopted the second-order approximation $\mathbf{v} \cong \overline{\mathbf{v}}$ and $\vartheta \cong \overline{\vartheta}$, the bar indicating a volume average over Ω, and $\vartheta_h = \vartheta_h(y)$ indicating the hydrostatic (equilibrium) temperature distribution. Thus, for a fluid of kinematical viscosity v and heat conductibility λ, the Reynolds number is defined as $Re = u_* H/v$, H being the depth and u_* the buoyancy reference velocity, the Prandtl number is $Pr = c_p\mu/\lambda$, the Rayleigh number is $Ra = g\beta H\Delta\vartheta/u_*^2$, being $\Delta\vartheta$ the equilibrium temperature difference. For a given known distribution of the velocity $\{\mathbf{v}^n, \mathbf{v}^{n-1}\}_C$ and temperature $\{\vartheta^n, \vartheta^{n-1}\}_C$ fields, Equation (39) can be first integrated in time by means of the AB/CN discretization since, typically, the discrete equation for the temperature is in the similar form of the scalar equation (36), rewritten for three-dimensions. Then, the updated temperature field $\{\vartheta^{n+1}\}_C$ is used for performing the time-discretization of the buoyancy term in (38) by means of the trapezoidal formula and the projection method can be performed.

As the *initial conditions* are concerned, a linear distribution $\vartheta(\mathbf{x}, 0) = y$ of the non-dimensional temperature is prescribed along with a zero velocity field. The *boundary conditions* are prescribed as follows. At $y = 0$ it is assumed that no-slip conditions are in effect, i.e. $u(x, 0, z, t) = v(x, 0, z, t) = w(x, 0, z, t) = 0$ and the temperature is fixed to $\vartheta(x, 0, z, t) = 0$. At $y = 1$ it is assumed that there is an interface with a different ambient producing heat exchange. However, no deformation of the interface is allowed and vanishing tangential stress are prescribed, i.e. $v(x,1,z,t)=0$, $(\partial u/\partial y)|_{x,1,z,t}=(\partial w/\partial y)|_{x,1,z,t}=0$. The interfacial heat flux is taken into account by considering the Fourier law and expressing the Neumann boundary conditions as $(\partial\vartheta/\partial y)|_{(x,1,z,t)}=-q_*H/\lambda\Delta\vartheta \triangleq -Nu$, where Nu is the Nusselt number, q_* being the applied flux prescribed to produce a cooling of the fluid. Moreover, periodic boundary conditions are applied along x and z directions.

In order to analyse the performances of the proposed procedure, the numerical results are illustrated while considering two basic solutions, the first one concerning the APM and the second the DPM formulations. Thus, the cases are subdivided in two classes of solutions according to:

Case A: Solutions obtained without solving the second elliptic equation that is only the first-order corrections (24) are used. Hence, the class of APM formulations is considered when the capital letter A is used.

Case B: Solutions obtained by solving the two-steps projection equation, that is the second-order corrections (28) are used. Hence, the class of DPM formulations is considered when the capital letter B is used.

Furthermore, each one of the above cases is then further subdivided in two sub-cases corresponding to different discretizations of the convective term. Specifically, the use of the normal-to-face velocities accords to the cases of the traditional or hybrid non-staggered grids:

Case a: The convective fluxes in Equation (10) are computed while exploiting only a linear interpolation of the velocity values in the FV centre. That is the staggered sets

$$\begin{aligned}&\{\hat{u}^2\}_f, \{\hat{v}^2\}_f, \{\hat{w}^2\}_f, \{\hat{u}\hat{w}\}_f, \{\hat{u}\hat{v}\}_f, \{\hat{v}\hat{w}\}_f\\ &\quad = N[\{u^2, v^2, w^2, uw, uv, vw\}_C]\end{aligned} \tag{40}$$

are employed. As an explicit example, the convective flux component of Equation (8), corresponding to the set $\{\hat{u}^2\}_f$, is computed by means of the mean value formula according to

$$\begin{aligned}\frac{1}{|\Omega_{ijk}|}\int_{z_k^-}^{z_k^+} \mathrm{d}\zeta \int_{y_j^-}^{y_j^+} (u^2|_{x_i^+} - u^2|_{x_i^-})\,\mathrm{d}\eta &\cong \frac{1}{\Delta x h_y \Delta z}[(\hat{u}^2)_{i+1/2,j,k} - (\hat{u}^2)_{i-1/2,j,k}]h_y\Delta z\\ \cong \frac{1}{\Delta x}\left[\frac{(u^2)_{i+1,j,k}+(u^2)_{i,j,k}}{2} - \frac{(u^2)_{i,j,k}+(u^2)_{i-1,j,k}}{2}\right] &= \frac{(u_{i+1,j,k})^2-(u_{i-1,j,k})^2}{2\Delta x}\end{aligned} \tag{41}$$

This approach is the one referred to here as traditional non-staggered grid [6, 15, 16] but without adopting the MIM or any other artificial dissipation terms. One can easily see that the large stencil in (41) can produce local oscillations. However, in general, the normal-to-face velocities in (40) can or cannot be divergence-free depending on which one between the main case B or A is in effect, respectively.

Case b: The convective fluxes in Equation (10) are computed by exploiting directly the MAC-like normal velocities. That is, the main-diagonal discrete fluxes are symbolically written as

$$\{u^2\}_f, \{v^2\}_f, \{w^2\}_f = \{N[\{u^*, v^*, w^*\}_C] - G[\{\phi^{n+1}\}_C]\}^2 \tag{42}$$

wherein only the MAC-like velocities, see Equations (23), are used, whereas the out main-diagonal discrete fluxes writes as

$$\begin{aligned}\{u\hat{v}\}_f, \{u\hat{w}\}_f &= \{N[\{u^*\}_C] - G[\{\phi^{n+1}\}_C]\}N[\{v,w\}_C]\\ \{v\hat{u}\}_f, \{v\hat{w}\}_f &= \{N[\{v^*\}_C] - G[\{\phi^{n+1}\}_C]\}N[\{u,w\}_C]\\ \{w\hat{u}\}_f, \{w\hat{v}\}_f &= \{N[\{w^*\}_C] - G[\{\phi^{n+1}\}_C]\}N[\{u,v\}_C]\end{aligned} \tag{43}$$

wherein both MAC-like and interpolated velocities are used. As a practical example of the differences existing from case a, the same flux component (41) rewrites now directly by using (42) as

$$\frac{1}{|\Omega_{ijk}|}\int_{z_k^-}^{z_k^+} \mathrm{d}\zeta \int_{y_j^-}^{y_j^+} (u^2|_{x_i^+} - u^2|_{x_i^-})\,\mathrm{d}\eta \cong \frac{1}{\Delta x h_y \Delta z}[(u^2)_{i+1/2,j,k} - (u^2)_{i-1/2,j,k}]h_y\Delta z = \frac{(u_{i+1/2,j,k})^2 - (u_{i-1/2,j,k})^2}{\Delta x} \tag{44}$$

where, by exploiting (23), only the MAC-like staggered velocity set $\{u\}_f$ is used. Conversely, an out main-diagonal term, for example the set $\{u\hat{v}\}_f = \{N[\{u^*\}_C] - G[\{\phi^{n+1}\}_C]\}N[\{v\}_C]$ in (43), allows us to write

$$\begin{aligned}&\frac{1}{|\Omega_{ijk}|}\int_{z_k^-}^{z_k^+} \mathrm{d}\zeta \int_{y_j^-}^{y_j^+} [(uv)|_{x_i^+} - (uv)|_{x_i^-}]\,\mathrm{d}\eta\\ &\cong \frac{1}{\Delta x h_y \Delta z}[(u\hat{v})_{i+1/2,j,k} - (u\hat{v})_{i-1/2,j,k}]h_y\Delta z\\ &\cong \frac{u_{i+1/2,j,k}(v_{i+1,j,k} + v_{i,j,k}) - u_{i-1/2,j,k}(v_{i,j,k} + v_{i-1,j,k})}{2\Delta x}\end{aligned} \tag{45}$$

where the hybrid product between MAC-like and interpolated velocities product appears. One can see that, differently from (41), this time the stencil is always compact. This formula accords to what is also proposed in References [13, 16, 17] since the used normal-to-face velocities are always divergence-free independently from using the case A or B.

From now on, while illustrating the results, the four cases are recalled by adopting the simple nomenclature *Aa*, *Ab*, *Ba* and *Bb*.

7.2. Numerical results

The simulations are performed only for the specific case of laminar flow and weak stratification. Thus, the non-dimensional parameters are fixed to $Nu = 600$, $Pr = 1$, $Ra = 2$, and a moderate Reynolds number, i.e. $Re = 30$, is prescribed. Figure 5 while describing a picture of the thermally buoyancy-driven motion, helps us in understanding how the solution generally behaves. In particular, a series of temporal snapshots each one representing five temperature

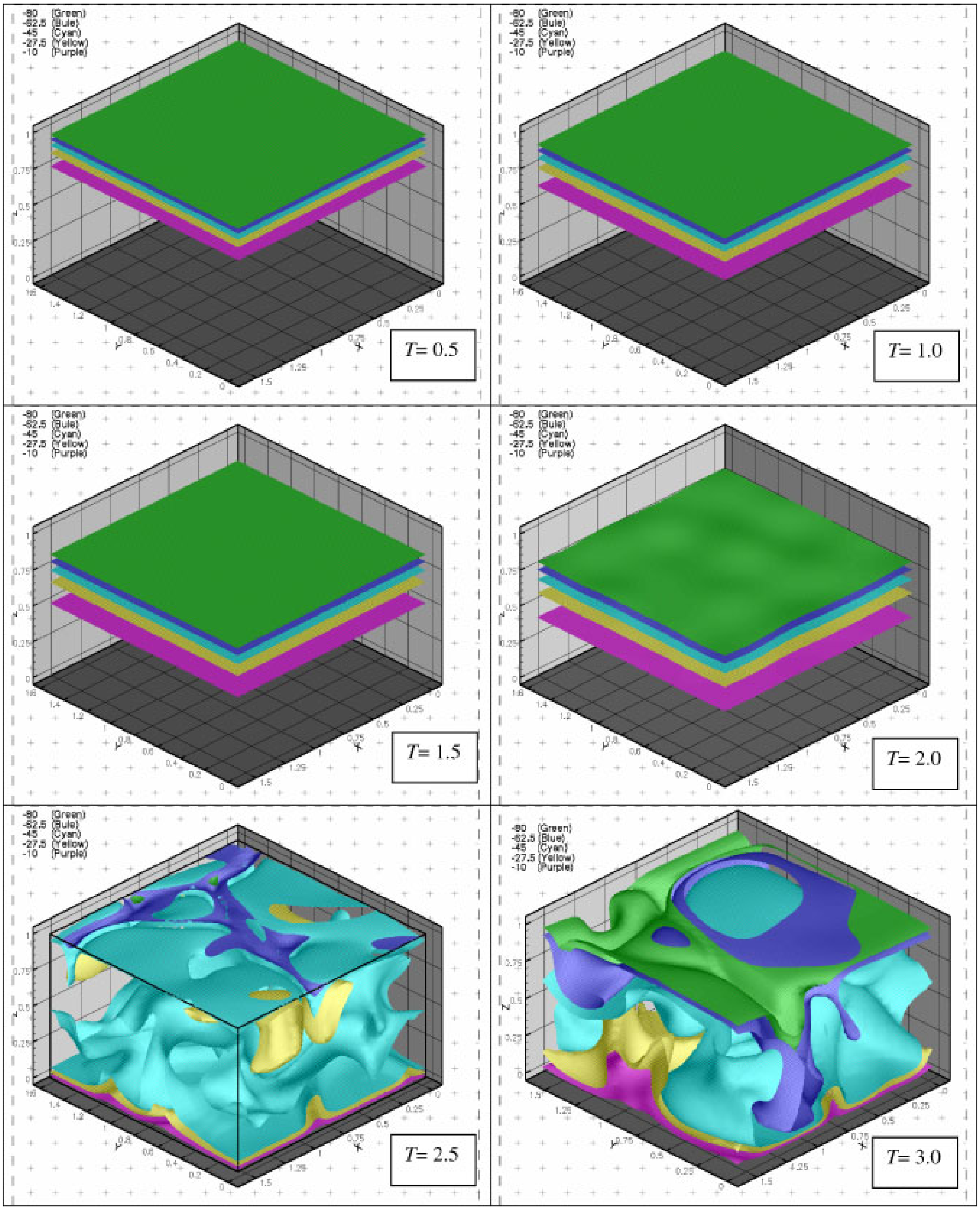

Figure 5. Iso-surfaces of temperature in the buoyancy-driven flow. Snapshots of the initial time-evolution of thermal boundary layer and onset of the instability at $T \approx 2$.

iso-surfaces is reported. The sequence describes that, starting from the initial hydrostatic equilibrium condition, the heat flux imposed at the upper interface causes the cooling of the fluid that onset the motion and increases the thickness of the thermal boundary layer. According to the Rayleigh–Bénard flows, it can be seen that there is a first phase dominated by the linear diffusion of the temperature in a practically unperturbed flow until to the time $T \approx 2$ at which instability starts. When the boundary layer becomes sufficiently ample, the convective motion starts and dominates the flow with appearance of thermal plumes. Laminar conditions are evident by inspecting the large dimension of the flow structures conversely, a typical case of turbulence in ocean, would similarly reproduce the same buoyancy mechanism however, while creating a well wider range of characteristic flow scales.

Initially, the comparisons of the results are illustrated in the case in which the domain V is discretized by using $21\times28\times21$ volumes while adopting a cosine law stretching along y (such that, near the interface at $j = m - 1$, the minimum mesh width $\min(h_y) \approx 1.57\times10^{-3}$ is obtained) and setting $\Delta t = 2\times10^{-5}$. Both elliptic equations are solved by means of an optimized SOR procedure, the first one stopped at a tolerance of 10^{-9}, the second at 10^{-6}, to be reached by the L_2 norm of the residual. Clearly, this means that the DPM procedure does not ensure the continuity to be satisfied up to machine accuracy but it stays limited within the chosen tolerance on the residual.

Owing to the unsteady character of this flow, in order for a clear comparison of the four cases to be highlighted, some suitable integral quantities are monitored in time. Specifically, they are:

- — the volume averaged kinetic energy that is subdivided in its horizontal, i.e. $(0.5/|V|) \int_V (u^2 + w^2)\,\mathrm{d}V$, and vertical, i.e. $(0.5/|V|) \int_V v^2\,\mathrm{d}V$, contributions (Figure 6);
- — the total continuity error, i.e. the sum of the (26), i.e. $D[N[\{u^{n+1}, v^{n+1}, w^{n+1}\}_C]]$, over all the FVs (Figure 7).

Figure 6 highlights the already commented behaviour, starting from the initial equilibrium condition, the first phase is dominated by the linear diffusion of the temperature until to the time $T \approx 2$ with a vanishing contribution of kinetic energy. However, oscillations in the total continuity are already visible in Figure 7, highlighting the intensity of non-divergent line modes along y. Clearly, the DPM well controls such oscillations. When the thermal boundary layer becomes sufficiently large and the convective motion is onset, $T > 2$, the kinetic energy rapidly increases.

It is worthwhile observing that, regardless of using APM or DPM procedures, both cases Aa and Ba produced solutions that become numerically unstable just after the onset of the convective regime although in Ba, owing to the use of the second elliptic equation, there is a small continuity error. Thus, it is plausible to deduce that the traditional non-staggered discretization a of the convective fluxes is responsible for generating high frequencies errors (contributing to the aliasing errors) that lead to the numerical instability eliminating any benefit of the second elliptic correction. This fact accords to the structure of the discrete flux operators acting on large stencil, e.g. see Equation (41), that allows the generation of spurious high frequency modes. Therefore, it seems advisable to use always the normal-to-face velocity (23), by using the hybrid non-staggered grid, whilst the traditional non-staggered one must be avoided.

Conversely, both cases performed on to the hybrid staggered grid, Ab (APM) and Bb (DPM), appear energy-stable, the simulations being continued for a time greater than that

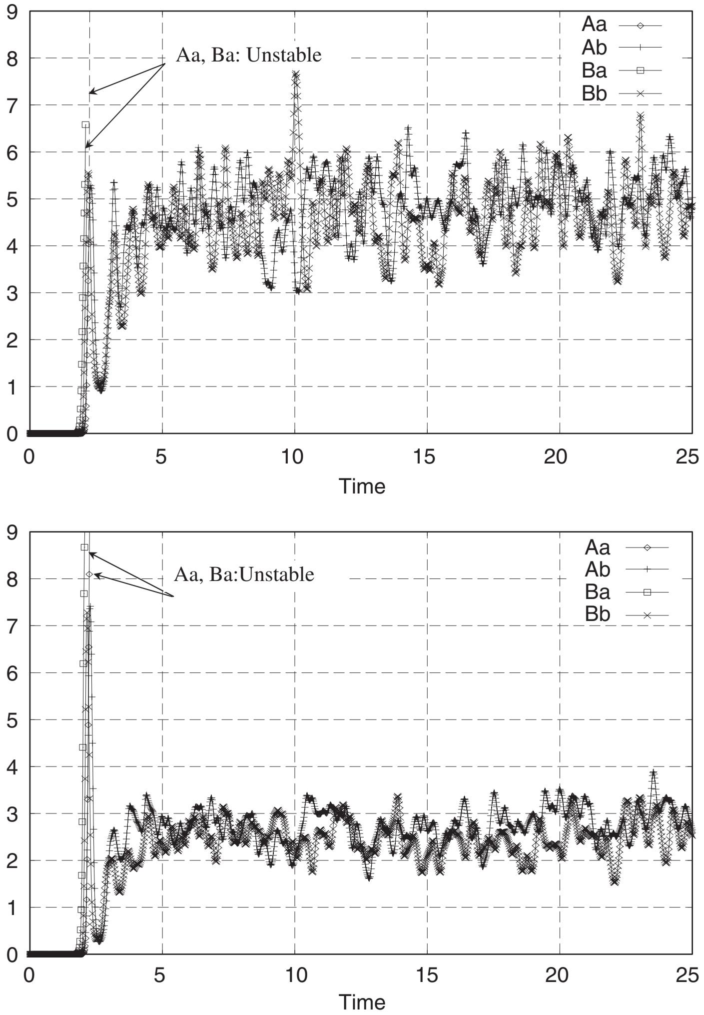

Figure 6. Buoyancy-driven flow on 21×28×21 volumes. Time-evolution of the horizontal (top) and vertical (bottom) contributions of the volume averaged kinetic energy.

reported in the figures. A finer observation to discern the best formulation is consequently necessary. However, while comparing the two cases, it is interesting to see that the case Ab produces a vertical component of the averaged kinetic energy greater in magnitude than in the case Bb, the differences in the horizontal one being less relevant. This issue hence deserves further investigations since it appears that, having used the same discretization of the convective fluxes, such difference should be attributed only to the false compressibility effect in the APM simulation. More specifically, it is useful to investigate if the continuity error in case Ab, highlighted in Figure 7, is mainly due to non-solenoidal modes along the vertical direction and is causing the discrepancy in the levels of the vertical kinetic energy.

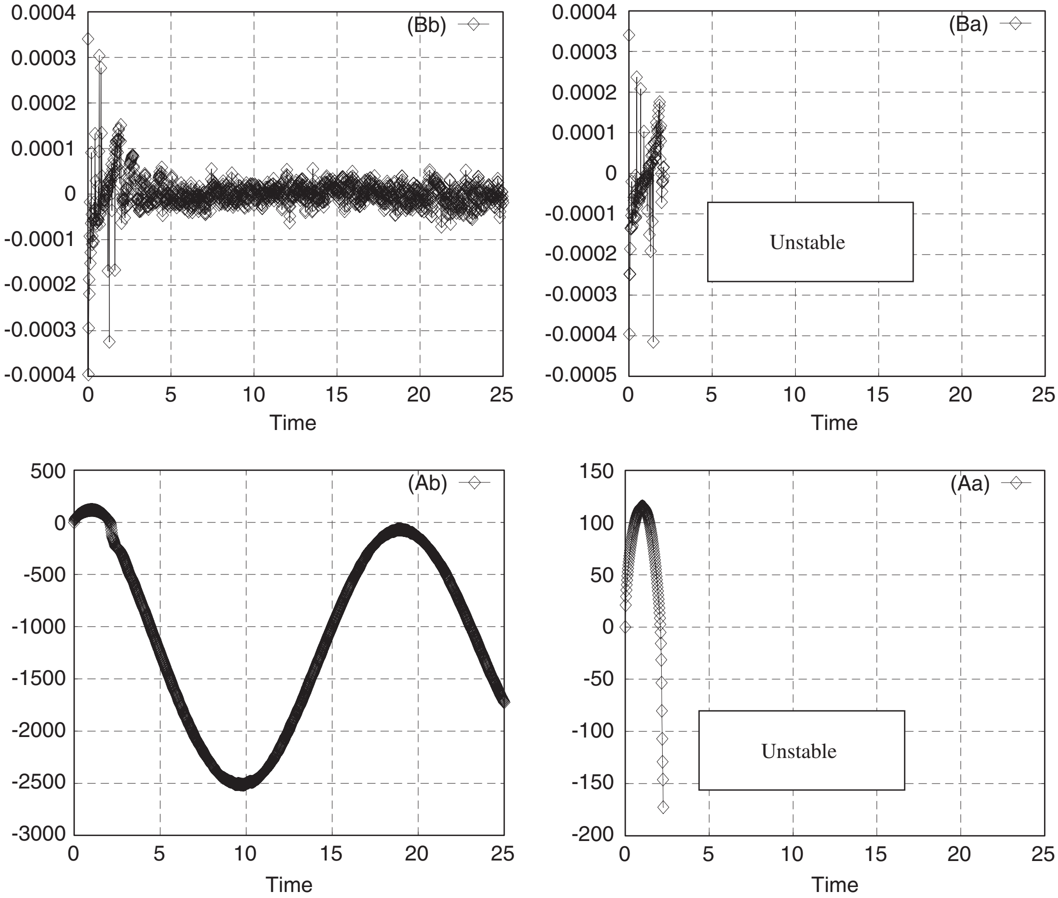

Figure 7. Buoyancy-driven flow on 21×28×21 volumes. Time-evolution of the volume averaged continuity errors resulting in the four cases.

Therefore, the velocities (Figures 8(a)–(c)) and temperature (8(d)) profiles along y, averaged in the homogeneous-flow (x, z) plane and reported at different times, i.e. $T = 1, 10, 20$, are illustrated and analysed. In Figure 8(a), the velocity profiles at $T = 1$ clearly illustrate that, although the magnitude of the oscillations appears generally small, the vertical velocity near the upper interface, where the grid points are more clustered, contains oscillations that are stronger in case Ab than those appearing in Bb. Despite of the compact stencil of the APM-based elliptic operator, the presence of non-solenoidal y-modes is remarkable whereas the DPM allows us to reduce the oscillations to a level controlled by the tolerance used in solving the second elliptic equation. At this time, the main convective motion is substantially absent, the diffusive thermal boundary layer is just been forming (the two averaged temperature profiles at $T = 1$ in Figure 8(d) are practically coincident). This feature shows that the DPM formulation successfully acts to locally smooth oscillations, without using dissipative-like operators. As a comparison, the goal pursued by projection-filter methods, proposed in

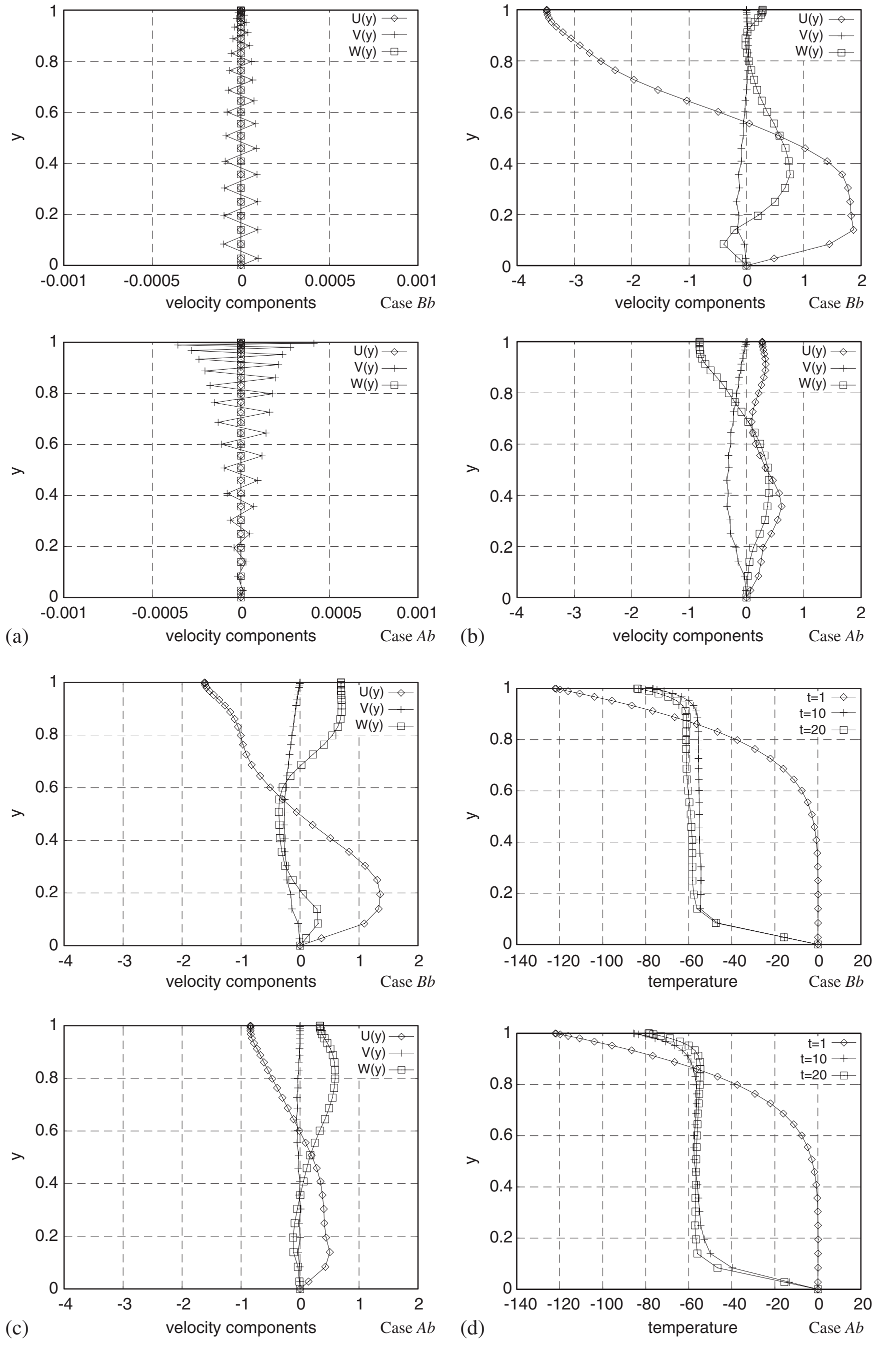

Figure 8. Buoyancy-driven flow on 21×28×21 volumes: (a) velocity profiles averaged in the (x,z) plane at $T=1$; (b) velocity profiles averaged in the (x,z) plane at $T=10$; (c) velocity profiles averaged in the (x,z) plane at $T=20$; and (d) time evolution of the temperature profiles, averaged in the (x,z) plane at $T=1,10,20$.

Reference [14], is similar but requires locally adding a dissipation-like operator that degrades the formal accuracy. Further information can be deduced during the time evolution since, regardless of the moderate Reynolds number, the flow pictures become very different in the two cases. Specifically, by looking at Figures 8(b) and (c), it appears that the averaged horizontal velocity component $\mathrm{U}(y)$ is substantially greater in case Ab than in Bb. Thus, the convective motion is more energized in the homogeneous plane. The temperature profiles in Figure 8(d) illustrate a particular issue observable during the time evolution from $T = 10$ to 20. Examining case Ab, it clearly appears that the profile is no longer monotone at $T = 20$ showing also an inversion from the behaviour at $T = 10$. Conversely, the profile is always monotone and progressively diminishing in the case Bb. This discrepancy is rather relevant and someway surprising if one considers the fact that the non-dimensional parameters are rather moderate and laminar flow condition should minimize the discrepancies. Remembering that, if the continuity equation is not well resolved, as happens in the APM, the term $p\underline{\nabla} \cdot \mathbf{v}$ acts as a source term in the kinetic energy equation, which is then converted in thermal energy, the difference in the evolution of the temperature profiles could be caused by this spurious effect. Hence, a deeper analysis seems necessary and, for the sake of conciseness, one now focuses only on the energy-stable cases Ab and Bb that are those using the hybrid non-staggered grid.

In order to investigate further the salient features of the DPM formulation as well as to assess the causes of discrepancies in the previous results, a grid-refinement should help us in understanding the mechanism that generates this effect. Thus, two other runs have been performed by refining the domain discretization while using $50 \times 50 \times 50$ volumes, the stretching being only along the vertical direction (the minimum vertical mesh size near the interface becomes $\min(h_y) \approx 4.93 \times 10^{-4}$). The same non-dimensional parameters and time-step (i.e. now the Courant number results increased) as well as the same tolerance for the two elliptic solvers are used. This way, it is supposed to highlight the sensitivity of the solution with respect only to the mesh size. In fact, on one hand, one reduces the (spatial) continuity error in the APM formulation, see Equations (25), (27), on the other hand, owing to the increase in the Courant number and the reduction of the cell-based Reynolds number, the stability region of the linear AB/CN equation (see Figure 3) highlights a more critical constraint on the integration parameters. Of course, this stability restriction applies for both APM and DPM formulations, thus one can assess the different behaviour exclusively in terms of the continuity error.

However, despite of the reduction of the continuity error, it can be seen from the evolution of the kinetic energy levels reported in Figure 9 that the case Ab (APM) becomes numerically unstable at $T \approx 5$ whilst the case Bb (DPM) has no stability problem. Instability seems to start mainly from the vertical energy contribution whereas the horizontal one increases but while staying still in the limits. This instability is associated to the presence of non-divergent line modes of velocities in the vertical direction close to the interface (for the sake of brevity not reported), such oscillations being rapidly amplified owing to the more critical stability constraint. Conversely, the velocity profiles reported in Figure 10 confirm that the DPM is oscillation-free at $T = 1$ and the other pictures illustrate the time evolution at $T = 10, 20$. Finally, the time evolution of the temperature profiles are shown in Figure 10(d) and it confirms the monotonic behaviour already observed on the coarse grid.

Therefore, one can assess that, by using the second elliptic solver, the DPM formulation takes advantage in terms of both accuracy and improvement of the stability features. Again,

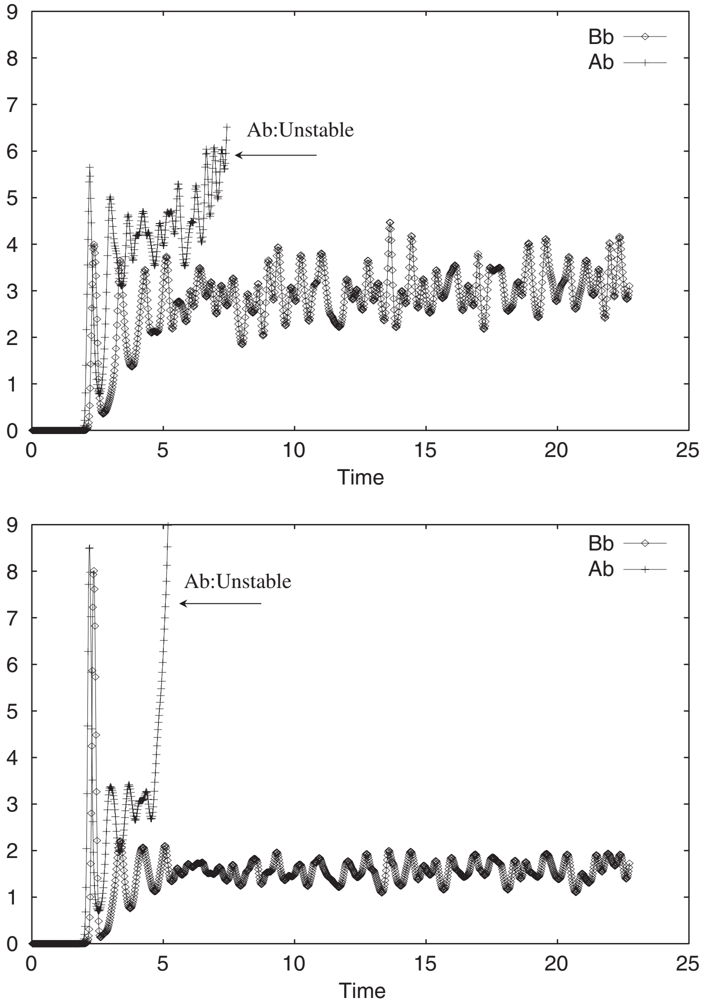

Figure 9. Buoyancy-driven flow on 50×50×50 volumes and $\Delta t = 2\times10^{-5}$. Time-evolution of the horizontal (top) and vertical (bottom) contributions of the volume averaged kinetic energy.

the theoretical linear stability analysis that was performed in Section 6 must be considered only as an indication since the non-linear character of NS equations generally produces more critical stability constraints. Of course, one cannot generalize this result by stating that the case Ab is unconditionally unstable, but the fact was highlighted that there exists a clear relation between continuity errors, generation of non-solenoidal velocity modes and stability. All the analysed methods are formally second-order accurate but, since accuracy order is only an asymptotic estimate, it is not surprising that for a fixed mesh size there are differences in the resulting results. Now these differences appeared also on the stability of the computation.

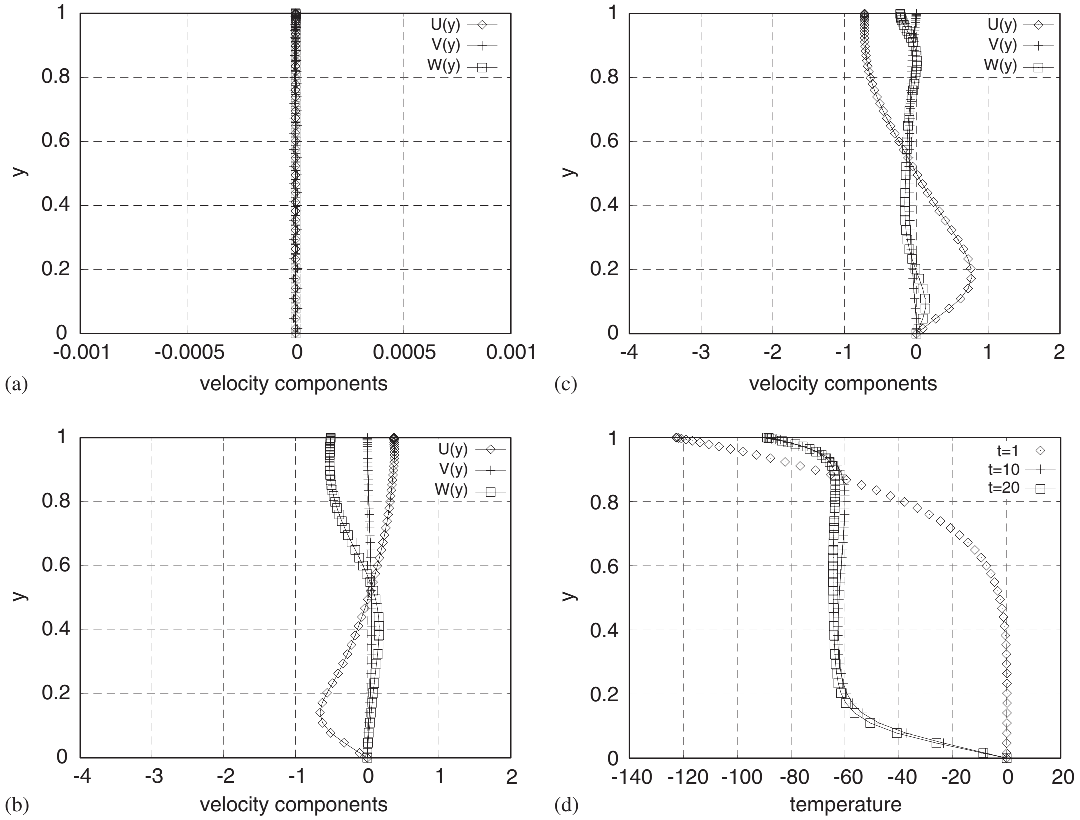

Figure 10. Buoyancy-driven flow on 50×50×50 volumes and $\Delta t = 2\times10^{-5}$ for the case Bb: (a) velocity profiles averaged in the (x,z) plane at $T = 1$; (b) velocity profiles averaged in the (x,z) plane at $T = 10$; (c) velocity profiles averaged in the (x,z) plane at $T = 20$; and (d) time evolution of the temperature profiles, averaged in the (x,z) plane, at times $T = 1, 10, 20$.

8. CONCLUDING REMARKS

This study explored some corrective methodologies that can be applied on a second-order accurate Finite Volume method on non-staggered grids in order for the continuity constraint to be ensured up to machine accuracy while not adding dissipation-like terms. In fact, this study is part of a more general research concerning both the direct numerical simulation (DNS) and the large eddy simulation (LES) of oceanographic flows for which buoyancy, wind stress, Coriolis acceleration are simultaneously present and drive turbulence in the marine environment (e.g. mixed layer, Langmuir circulation). Therefore, the goal is to implement an energy stable formulation that is suitable in simulating incompressible turbulence while avoiding false effects in the energy dynamics due to compressibility errors. Especially the LES approaches require a careful resolution of the variables in the characteristic spectrum range since the modelling procedure for computing the sub-grid scale terms (e.g. the dynamic procedure) both for the momentum and thermal energy equation, e.g. see References [12, 22], can be dramatically affected by numerical errors.

Therefore, it was analysed what happens by using the exact and approximate projection method and, since the standard exact projection method strongly suffers presence of non-divergent spurious modes whereas the approximate one does not satisfy the mass conservation, a strategy is suggested to obtain an exact projection but in two consecutive steps (DPM). Actually, other methods such as the MIM or the projection-filter method prevent spurious oscillations but adds artificial dissipative terms that can alter the resolved energy spectrum whilst the present method is based only on a potential correction. Thus, a second elliptic equation, suitably derived from the projection of cell-centred intermediate velocity, is proposed. It is worthwhile observing that the additional computational effort (although it is not necessary to use the same high tolerance level of the first solver) is justified by the fact that otherwise one should use a very refined grid as well as a small time step to reduce the errors of the APM.

The new DPM proposal was addressed and the main features in terms of stability and accuracy are illustrated by means of the Taylor vortex decaying test-case. Eventually, the DPM formulation has been developed for solving a laminar unsteady buoyancy-driven flow and hybrid and traditional non-staggered grid collocations have been compared. The results obtained for a moderate Reynolds and Rayleigh numbers, illustrated the better quality of the present formulation.

At present, DNS and LES simulations of turbulent oceanographic flows with second-order formulations are currently under investigation [23]. Furthermore, a three-dimensional extension of the higher order formulation [24] is also in progress. Even if many disquisitions in this paper are valid when one speaks of second-order central discretizations, the local mass conservation guaranty and the absence of spurious non-solenoidal modes are requisite that remain fundamental also for higher order accurate discretizations.

ACKNOWLEDGEMENTS

This study is part of a more general research on LES methodologies and oceanographic turbulence modelling supported by a Grant of the CINECA consortium (Italy). Other participants of this research are, in alphabetical order, A. Aprovitola, V. Botte, G. De Stefano, D. Iudicone, that I thank for some useful advices.

REFERENCES

1. Gresho PM. Incompressible fluid dynamics: some fundamental formulation issues. *Annual Review of Fluid Mechanics* 1991; **23**:413–453.
2. Vinokur M. An analysis of finite-difference and finite-volume formulations of conservation laws. *Journal of Computational Physics* 1989; **81**:1–52.
3. LeVeque RJ. *Finite Volume Methods for Hyperbolic Problems*. Cambridge University Press: Cambridge, 2002.
4. Harlow FH, Welch JE. Numerical calculation of time-dependent viscous incompressible flow of fluid with a free surface. *Physics of Fluids* 1965; **8**:2182–2189.
5. Iannelli P, Denaro FM, De Stefano G. A deconvolution-based fourth order finite volume method for incompressible flows on non-uniform grids. *International Journal for Numerical Methods in Fluids* 2003; **43**:431–462.
6. Ferziger JH, Peric M. *Computational Methods for Fluid Dynamics*. Springer: Berlin, 2002.
7. Sotiropoulos F, Abdallah S. The discrete continuity equation in primitive variable solutions of incompressible flow. *Journal of Computational Physics* 1991; **95**:212–227.
8. Dormy E. An accurate treatment of pressure for collocated variables. *Journal of Computational Physics* 1999; **151**:676–683.

9. Chorin AJ. Numerical solution of the Navier–Stokes equations. *Mathematics of Computation* 1968; **22**: 745–762.
10. Kim J, Moin P. Application of a fractional-step method to incompressible Navier–Stokes equations. *Journal of Computational Physics* 1985; **59**:308–323.
11. Brown DL, Cortez R, Minion ML. Accurate projection methods for the incompressible Navier–Stokes equations. *Journal of Computational Physics* 2001; **168**:464–499.
12. Iannelli P, Denaro FM. Analysis of the local truncation error in the pressure-free projection method for the Navier–Stokes equations: a new accurate expression of the boundary conditions. *International Journal for Numerical Methods in Fluids* 2003; **42**:399–437.
13. Almgren AS, Bell JB, Szymczak WG. A numerical method for the incompressible Navier–Stokes equations based on an approximate projection. *SIAM Journal on Scientific Computing* 1996; **17**:358–369.
14. Rider WJ. Filtering non-solenoidal modes in numerical solutions of incompressible flows. *International Journal for Numerical Methods in Fluids* 2003; **28**:789–814.
15. Rhie CM, Chow WL. Numerical study of the turbulent flow past an airfoil with trailing edge separation. *AIAA Journal* 1983; **21**:1525–1532.
16. Zang Y, Street RL, Koseff JR. A non-staggered grid, fractional step method for time-dependent incompressible Navier–Stokes equations in curvilinear coordinates. *Journal of Computational Physics* 1994; **114**:18–33.
17. Kim D, Choi H. A second-order time-accurate Finite Volume method for unsteady incompressible flow on hybrid unstructured grids. *Journal of Computational Physics* 2000; **162**:411–428.
18. Denaro FM. On the application of the Helmholtz–Hodge decomposition in projection methods for the numerical solution of the incompressible Navier–Stokes equations with general boundary conditions. *International Journal for Numerical Methods in Fluids* 2003; **43**:43–69.
19. Denaro FM. Time-accurate intermediate boundary conditions for large eddy simulations based on projection methods. *International Journal for Numerical Methods in Fluids* 2005; **48**:869–908.
20. Denaro FM, Sarghini F. 2D transmitral flows simulation by means of the immersed boundary method on unstructured grids. *International Journal for Numerical Methods in Fluids* 2002; **38**:1136–1157.
21. Guy RD, Fogelson AL. Stability of approximate projection methods on cell-centered grids. *Journal of Computational Physics* 2005; **203**:517–538.
22. Zikanov O, Slinn SN, Dhanak MR. Turbulent convection driven by surface cooling in shallow water. *Journal of Fluid Mechanics* 2002; **464**:81–111.
23. Denaro FM, De Stefano D, Iudicone D, Botte V. Simulazione numerica LES dell'effetto del raffreddamento in mare. *XVII Congresso AIMETA*, Firenze, 2005
24. Aprovitola A, Denaro FM. On the application of congruent upwind discretizations for large eddy simulations. *Journal of Computational Physics* 2004; **194**(1):329–343.